Satellite-based Analysis of Ocean-Surface Stress across the Ice-free and Ice-covered Polar Oceans

Chao Liu[1], Lisan Yu[1]

[1]Woods Hole Oceanographic Institution, Woods Hole, MA, USA

Correspondence to: Chao Liu (chao.liu@whoi.edu)

Abstract. Ocean-surface stress is a critical driver of polar sea ice dynamics, air-sea interactions, and ocean circulation. This work provides a daily analysis of ocean-surface stress on 25-km Equal-Area Scalable Earth (EASE) Grids across the ice-free and ice-covered regions of the polar oceans (2011-2018 for Arctic, 2013-2018 for Antarctic), covering latitudes north of 60°N in the Arctic and south of 50°S in the Antarctic and Southern Ocean. Ocean-surface stress is calculated using a bulk parameterization approach that combines ocean-surface winds, ice motion vectors, and sea surface height (SSH) data from multiple satellite platforms. The analysis captures significant spatial and temporal variability in ocean-surface wind stress and the resultant wind-driven Ekman transport, while providing enhanced spatiotemporal resolution. Two sensitivity analyses are conducted to address key sources of uncertainty. The first addresses the fine-scale variability in SSH fields, which was mitigated using a 150-km Gaussian filter to smooth three-day SSH datasets and enhance compatibility with the other monthly product, followed by linear interpolation to achieve daily resolution. The second investigates uncertainty in the ice-water drag coefficient, which revealed that variations in the coefficient have a proportional influence on the computed ocean-surface stress under the tested conditions. These uncertainties are most pronounced during winter, with median values reaching 20% in the Arctic and 40% in the Southern Ocean. Validation efforts using Ice-Tethered Profiler velocity records revealed weak to moderate correlations with satellite-derived stress (r = 0.4–0.8) between observed surface velocities and satellite-derived estimates (Ekman + geostrophic) at daily resolution, with significantly improved agreement when averaged to weekly means. This dataset is publicly available at https://doi.org/10.5281/zenodo.14750492 (Liu & Yu, 2024).

1 Introduction

Earth's polar regions have undergone profound changes over the past decades, with sea ice playing a central role in the polar climate system. By modulating heat, momentum, and freshwater exchanges at the atmosphere-ice-ocean boundary, sea ice directly influences global climate dynamics (Meehl, 1984; Stammerjohn et al., 2012). In the Arctic, rapid sea ice decline has transitioned the region from predominantly thick, multiyear ice to thinner, more dynamic ice, with increased interannual variability (Comiso et al., 2008; Stroeve and Notz, 2018; Moore et al., 2022; Babb et al., 2022). Meanwhile, Antarctic sea ice trends have shown greater complexity, with a modest long-term increase observed until the mid-2010s, followed by a record loss in 2017 and a subsequent continued decline (Liu et al., 2004; Parkinson, 2019; Turner et al., 2022; Purich & Doddridge, 2023). These changes in sea ice extent and thickness have significant implications for polar systems and global climate feedbacks, influencing the Arctic's ability to regulate planetary heat, as well as impacting marine ecosystem, carbon cycling, nutrient distribution, and thermohaline circulation (Talley, 2013; Campbell et al., 2019).

Atmospheric circulation is a primary driver of sea ice dynamics and variability. Geostrophic winds, for instance, account for over 70% of sea ice velocity variability (Thorndike and Colony, 1982; Maeda et al., 2020), while broader climate modes, including the Arctic Oscillation, Pacific Decadal Oscillation, and Southern Annular Mode, influence ice extent and distribution (Rigor et al., 2002; Park et al., 2018; Lefebvre et al., 2004). These wind-driven processes interact with sea ice to modify ocean-surface stress, impacting Ekman dynamics and the transport of heat, salt, and nutrients (Yang, 2006, 2009; Meneghello et al., 2018). This feedback mechanism, often described as the "ice-ocean governor" (Meneghello et al., 2017), plays an important role in regulating polar freshwater storage and circulation (Marshall and Speer, 2012; Abernathey et al., 2016; Ma et al., 2017).

Surface stress plays a pivotal role in driving Arctic Ocean circulation by mediating the transfer of momentum from the atmosphere to the ocean. In the Arctic, sea ice acts as a modulator of this momentum exchange, either dampening or amplifying the transfer depending on its concentration and mechanical properties. Recent projections indicate that as the Arctic climate warms, sea ice will become thinner and less extensive, leading to a more efficient transfer of wind energy to the ocean surface (Muilwijk et al., 2024). This enhanced momentum transfer is expected to accelerate surface currents, increase ocean kinetic energy, and intensify vertical mixing processes (Martin et al. 2014; Martin et al. 2016). However, current climate models exhibit considerable uncertainty in simulating these processes due to simplified representations of atmosphere-ice-ocean interactions. Therefore, developing observationally based surface stress products is essential for validating and improving model simulations, leading to more accurate predictions of future Arctic Ocean dynamics and their global implications.

To address the complexity of ice–ocean interactions, recent modeling advances have highlighted the pivotal role of sea ice form drag in governing momentum exchange at the ocean–ice–atmosphere interface. Tsamados et al. (2014) introduced a physically grounded parameterization of ice form drag that accounts for ice morphological features—such as ridges, floe edges, and melt pond geometry—and demonstrated that spatial and temporal variability in drag coefficients can substantially influence sea ice dynamics and the spin-up of the Arctic Ocean. Extending this approach, Sterlin et al. (2023) implemented a variable ice form drag scheme in the NEMO-LIM3 ocean–sea ice model and found that it exerts a pronounced control over

Despite significant advancements in understanding these processes, direct measurements at the ice-ocean interface remain limited, with most data concentrated in the Arctic's Canada Basin (Smith et al., 2019; Regan et al., 2019). Satellite remote sensing has been instrumental in addressing these gaps, providing open ocean-surface wind retrievals available since 1988 (Yu & Jin, 2014a) and tracking sea ice motions since 1978 (Cavalieri et al., 1996). Recent advances in satellite altimetry further enable high-resolution monitoring of sea surface height (SSH) changes, offering new insights into mesoscale ocean dynamics (Armitage et al., 2016, 2017; Prandi et al., 2021).

Building upon the concepts developed in previous studies (Yang, 2006, 2009; Meneghello et al., 2018), this analysis utilizes recent satellite-based datasets on wind, ice motion, and SSH to analyze ocean-surface stress across both ice-free and ice-covered polar seas. Specifically, we present a daily analysis of ocean-surface stress at 25-km resolution using Equal-Area Scalable Earth (EASE, see glossary in Table A1 for more details) Grids from 2011 to 2018 for Arctic and 2013-2018 for Antarctic, covering latitudes north of 60°N in the Arctic and south of 50°S in the Antarctic and Southern Ocean (Figure 1).

Section 2 provides a description of the satellite datasets used and processing steps, along with the methods for calculating ocean-surface stress and Ekman circulation. Section 3 presents the time-mean patterns and variability of the derived surface stress and Ekman pumping fields. Section 4 addresses quantification of uncertainties in the analysis, including sensitivity to the ice-water drag coefficient and comparisons of with in-situ data.

80
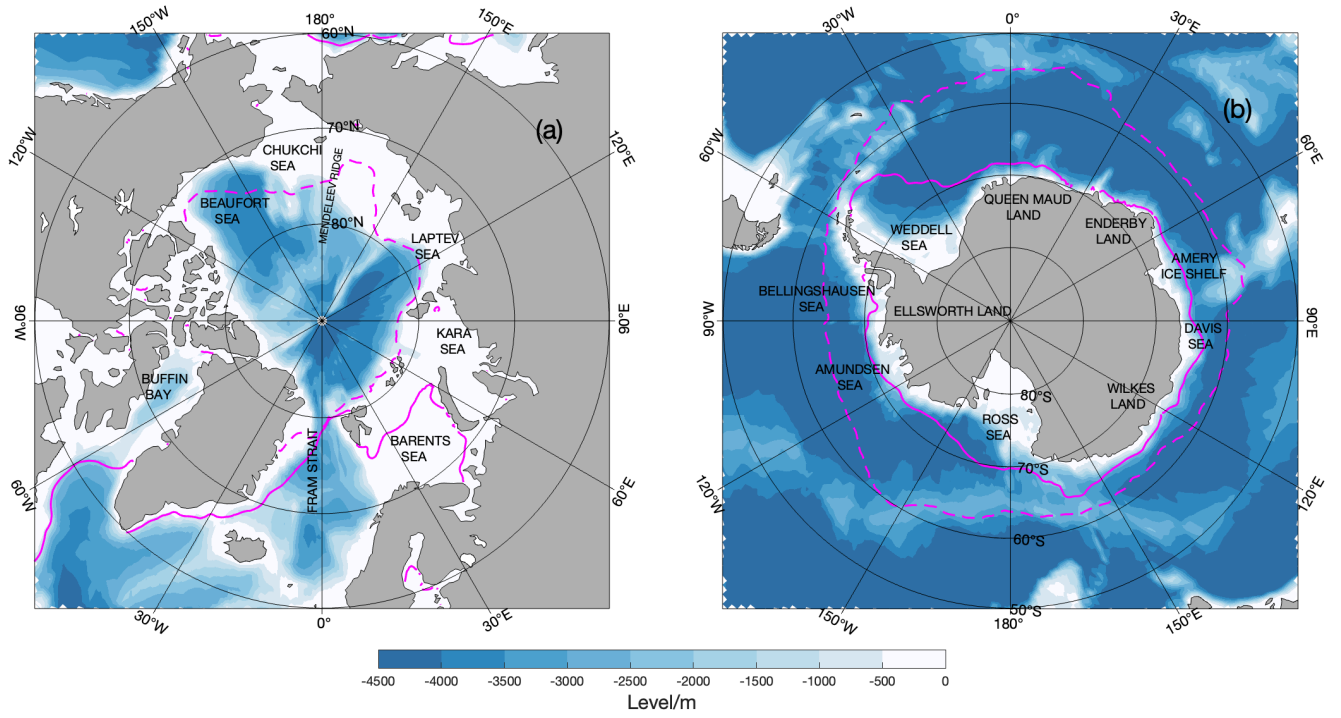
Figure 1: Study region in (a) Arctic and (b) Southern Oceans. Blue shading represents the bathymetry in meter. Solid and dashed magenta lines indicate the median sea ice extent boundaries for March and September, respectively, defined by areas with sea ice concentration.

2 Data, Method and Processing of the Analysis

2.1 Calculation of Ocean-Surface Stress and the Ekman Transport

The ocean-surface stress is estimated using the methodology proposed by Yang (2006, 2009), with modifications by Meneghello et al. (2018). The total ocean-surface stress (τ_o) is calculated as a weighted linear combination of ice–water stress (τ_{iw}) and air–water stress (τ_{aw}), based on the fractional sea ice concentration:

$$\tau_o = \alpha\tau_{iw} + (1 - \alpha)\tau_{aw} \tag{1}$$

where α is set to 0 for the ice-free surfaces (defined as sea ice concentration less than 15%) and 1 for ice-covered surfaces (defined as sea ice concentration exceeding 15%). The stresses τ_{iw} and τ_{aw} are parameterized using quadratic drag laws:

$$\tau_{iw} = \rho_w C_{D,iw}|U_{ice} - U_e - U_g|(\boldsymbol{U_{ice}} - \boldsymbol{U_e} - \boldsymbol{U_g}) \tag{2}$$

and

$$\tau_{aw} = \rho_a C_{D,aw}|U_{10}|\boldsymbol{U_{10}} \tag{3}$$

where U_{ice}, U_e, U_g, and U_{10} are the local ice motion, Ekman velocity, geostrophic velocity, and equivalent neutral wind at 10-m height, respectively. ρ_w = 1027.5 kg m^{-3} and ρ_a represent the densities of water and air. In this product, τ_{aw} is taken directly from existing satellite wind products (Yu and Jin 2014a, b).

98    $C_{D,iw}$ is the ice-water drag coefficient and $C_{D,iw} = 5.5 \times 10^{-3}$ is adopted in this product as it is a commonly recognized value.

99   It is worth noting that, due to the limited availability of direct observations, $C_{D,iw}$ is identified as a key source of uncertainty.

100   A sensitivity analysis is therefore provided in the following section to evaluate its potential impact.

101   In Equation (2), surface ocean velocity expressed as the sum of U_g and U_e. The representation of ocean surface stress is known

102   to be highly sensitive to the assumed surface velocity used in the drag formulation. A range of approaches has been employed

103   in past studies—incorporating U_e, U_g, or even assuming zero ocean motion—each with markedly different implications. For

104   instance, Zhong et al. (2018) showed that mean Ekman pumping in the Beaufort Sea can differ by over 50% depending on the

105   inclusion of geostrophic flow. Wu et al. (2021) reported similar sensitivities in the Nordic Seas, while earlier works by Zhong

106   et al. (2015) and Ma et al. (2017) further detailed the variability across Arctic regimes. As a result, stress-based diagnostics

107   remain sensitive to parameterization choices, and conclusions should be interpreted with that uncertainty in mind.

108   The geostrophic velocity U_g can be calculated from dynamic ocean topography datasets (McPhee 2013; Armitage et al. 2016,

109   2017). The Ekman velocity U_e, which moves at an angle of 45° to the right of the ocean-surface stress in the Northern

110   Hemisphere, is calculated as:

111   $$U_e = \frac{\sqrt{2}e^{-i(\pi/4)}}{f\rho_w D_e}\tau_o \qquad\qquad\qquad (4)$$

112   where f is the Coriolis parameter, and D_e is the Ekman layer depth (20 m, Meneghello et al., 2018). Since U_e and τ_o are

113   interdependent in Eqs. (1) and (4), a modified Richardson iteration method is applied to solve them iteratively until converge

114   is achieved, starting with $U_e = 0$ in the first iteration (Yang 2006).

115   Subsequently, the vertical Ekman velocity w_e can be calculated as follows:

116   $$w_e = \frac{1}{f\rho_w}\nabla \times \tau_o \qquad\qquad\qquad (5)$$

117   A positive w_e indicates upwelling, while a negative w_e corresponds to downwelling.

118

119   **2.2 Data Description**

120   The calculation of total ocean-surface stress (Eqs. (1)–(4)) requires the following input datasets: ocean-surface wind stress

121   (τ_{aw}), sea ice concentration (α), sea ice motion (U_{ice}), and dynamic topography for geostrophic velocity (U_g). A brief

122   description of each satellite-based dataset is given in Table 1.

123

124   **Table 1: Gridded satellite datasets used in the work.**

Variable	Source	Resolution	Period	Reference
Surface Wind Stress τ_{aw}	OAFlux2	Daily, 0.25°	1988-present	Yu & Jin, 2014a, 2014b
Ice Motion U_{ice}	Polar Pathfinder v4	Daily, 25 km	1978-2023	Tschudi et al., 2019

Geostrophic U_g	multi-altimeter dataset	3-Day, 25 km	2011-2021 (Arctic) 2013-2021 (Antarctic)	Prandi et al., 2021
Sea Ice Concentration α	NSIDC0051, v2	Daily, 25 km	1988-present	DiGirolamo et al., 2022

125

126 In this product, the air-water wind stress is taken from OAFlux2 (Yu & Jin, 2014a, 2014b), a satellite-derived 0.25-degree
127 gridded air-sea flux daily analysis (1988 to present) developed under the auspices of NASA's Making Earth System Data
128 Records for Use (MEaSUREs) program (Yu, 2019). OAFlux2 winds are synthesized from 19 active and passive satellite wind
129 sensors and wind stress are calculated from the Coupled Ocean-Atmosphere Response Experiment (COARE) bulk algorithm
130 version 3.6 (Fairall et al., 2003).

131 Daily sea ice motion vectors for the Arctic and Antarctic regions are obtained from the National Snow and Ice Data Center's
132 (NSIDC) Polar Pathfinder Daily 25 km EASE-Grid Sea Ice Motion Vectors, Version 4 (Tschudi et al., 2019, 2020), covering
133 the period from 1978 through 2023. The ice motion fields are derived from multiple sources, including passive microwave
134 radiometers (e.g., SSM/I, AMSR-E), visible and infrared sensors (e.g., AVHRR, MODIS), scatterometers (e.g., QuikSCAT),
135 drifting buoys (e.g., IABP), and atmospheric reanalysis winds. Feature-tracking algorithms are applied to sequential satellite
136 images to identify ice displacement, while optimal interpolation techniques combine the various data sources to produce daily
137 sea ice motion estimates. The resulting vectors represent sea ice displacement over a 24-hour period and are gridded onto a 25
138 km EASE grid 2.0 (EASE2).

139 Geostrophic velocity in the Arctic and Antarctic are obtained from the CLS/PML multi-altimeter combined Arctic/Antarctic
140 Ocean sea level dataset (Prandi et al., 2021). This dataset spans latitudes north of 50°N on a 25 km EASE2, with a temporal
141 resolution of one grid point every 3 days. Covering the Arctic from 2011 to 2021 and the Antarctic from 2013 to 2021, the
142 CLS dataset mitigates the spurious meridional signals often introduced by the longer sampling intervals of CryoSat-2
143 observations (Auger et al., 2022).

144 The Sea Ice Concentrations from Nimbus-7 SMMR and DMSP SSM/I–SSMIS Passive Microwave Data, Version 2 (NSIDC-
145 0051, Cavalieri et al., 1996; DiGirolamo et al., 2022) is used to define the daily ice boundary based on the 15% ice
146 concentration threshold. NSIDC-0051 provides a reliable, long-term record of sea ice concentration, making it valuable for
147 studying sea ice conditions and large-scale climate variability (Parkinson, 2019). Widely recognized for its accuracy, the
148 dataset is frequently used to validate and improve climate model simulations. The daily dataset is available from 1987 to the
149 present and provide a coverage on a 25 km resolution polar stereographic grid for the both polar regions.

150 The analysis period ends in 2018 to maintain consistency with the most reliable iteration of the ongoing refinement of OAFlux
151 wind product. While this choice limits the temporal extent, the framework itself remains flexible and can be readily extended

152 as newer, better-resolved datasets become available. With all considered, the study period for Antarctica is constrained to six
153 years (2013–2018), while an eight-year period (2011–2018) is maintained for the Arctic.

2.3 Data processing procedure

155 Using the methodology described in Eqs. (1)-(5) and the input data listed in Table1, the workflow for processing and analysing
156 data to calculate ocean-surface stress and derive vertical Ekman velocity is shown in Figure 2.

157
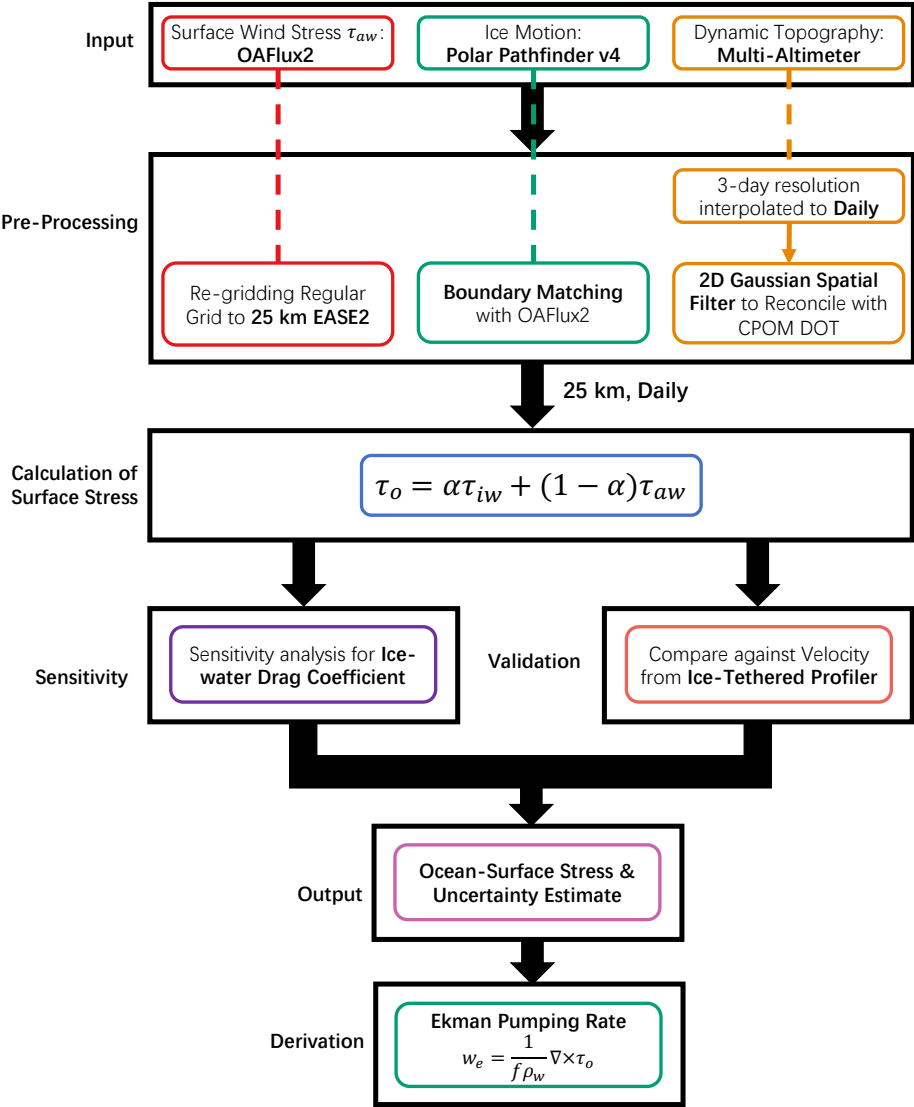
158 **Figure 2: Workflow for data processing and analysis to calculate ocean-surface stress and derive vertical Ekman velocity.**

All datasets are interpolated onto a common 25 km EASE grid format, providing uniform spatial resolution and facilitating consistent analysis across the Arctic and Antarctic regions. Although the discrepancies in sea-ice boundaries are very limited over 2011-2018 (less than 2% of total grids), ice concentration and motion data are adjusted to better align with OAflux2 wind stress. Noting that the 25 km resolution may introduce uncertainties near the 15% sea ice concentration boundary, as such coarse resolution can obscure sharp gradients in the marginal ice zone and misclassify mixed ice–water grid cells (e.g., Meier, 2005; Ivanova et al., 2015).

Temporal sampling frequency plays a critical role in determining the accuracy and interpretability of ocean surface stress estimates. Daily and sub-daily sampling is often needed to capture short-term variability in wind and sea ice motion, which directly affects transient stress fluctuations and high-frequency Ekman responses (Meneghello et al., 2018; Regan et al., 2020). Conversely, monthly-averaged fields may overly smooth dynamic features and obscure important stress events, particularly in regions with strong synoptic variability. In this context, the 3-day sampling of the CLS/PML altimetry product offers a useful compromise: it resolves large-scale mesoscale dynamics more consistently than monthly data while maintaining better signal-to-noise properties than noisy daily sea surface height reconstructions in ice-covered regions (Prandi et al., 2021). Given the limitations of satellite altimetry in the polar oceans, the CLS dataset provides a crucial improvement by reducing spurious meridional errors and enabling more consistent estimation of geostrophic velocities and their role in modulating surface stress (Auger et al., 2022). We revisit the implications of time-averaging choices for surface stress/derived velocity fields in Section 4.2.

While the CLS/PML product offers improved temporal resolution and geophysical realism at finer spatial scales, its use of multiple altimeters and interpolation techniques can introduce high-frequency structures that remain difficult to validate given the sparse in situ coverage at high latitudes (Prandi et al., 2021; Auger et al., 2022). In contrast, the CPOM Dynamic Ocean Topography (DOT) dataset (2003-2021) from the Centre for Polar Observation and Modelling (CPOM; Armitage et al., 2016, 2017), despite its coarser resolution and monthly cadence, has seen wider adoption and validation across climate-scale Arctic studies (e.g., Meneghello et al., 2018; Zhong et al., 2018; Lin et al., 2023), making it a valuable benchmark for cross-comparison. To reconcile the strengths of both datasets, we apply a two-dimensional Gaussian spatial filter to smooth CLS fields, aligning their effective resolution with CPOM and improving interpretability of large-scale patterns. This hybrid approach leverages the temporal detail of CLS while benefiting from the broader-scale reliability of CPOM, offering a more balanced foundation for stress estimation and error characterization in polar oceanographic applications.

We employed a 2D Gaussian filter with a standard deviation of 75 km to improve consistency and interpretability between CLS and CPOM DOT datasets, which have different resolutions and small-scale characteristics. A sensitivity test is conducted to determine the optimal filter radius, ranging from 50 km to 250 km. Smaller filters (e.g., <50 km) preserve small-scale variability but may complicate the interpretation of large-scale features, while larger filters (e.g., >250 km) can excessively smooth mesoscale processes, such as boundary currents, reducing the dataset's ability to capture key processes of polar dynamics.

192 To find the optimal filter size, a series of tests were conducted for 2011. The effectiveness of each filter setting is evaluated

193 using the Root Mean Squared Deviation (RMSD):

194 $$RMSD = \sqrt{\frac{1}{N}\sum_{i,j}\left(w_{e\ i,j} - w_{e_{ref,(i,j)}}\right)^2} \tag{6}$$

195 where w_e represents the local vertical Ekman velocity w_e derived from the CLS dataset, filtered with a specific Gaussian filter

196 size (e.g., 100 km, 150 km, etc.), and w_{ref} is the reference vertical Ekman velocity calculated using the CPOM dataset. N is

197 the total number of the grid points with sea ice coverage.

198 The unfiltered CLS dataset exhibits clear seasonal variations in RMSD, with values peaking at 25 cm/day during winter and

199 decreasing in summer (Figure 3a). Applying a Gaussian filter significantly enhances agreement with the CPOM dataset,

200 reducing RMSD by 10–15 cm/day for most of the year. However, in late summer the reduction is only 2–5 cm/day.

201 Increasing the filter size further enhances spatial agreement (Figure 3b). From no-filter to a 100 km filter, the annual mean

202 RMSD is reduced to 17 cm/day, and increasing the filter size to 150 km further lowers the RMSD to 15.5 cm/day. The standard

203 deviation of daily RMSD is also reduced by half with 150 km filter compared to the unfiltered results. However, larger filter

204 sizes (e.g. 200 km and 250 km) yield only marginal additional improvements. Therefore, the 150 km Gaussian filter is selected

205 as a practical and effective balance between preserving spatial features and minimizing small-scale variability for this work.

206 Figure 3c–h demonstrates the impact of varying filter sizes on the spatial structures of τ_o and w_e on March 15, 2011. Without

207 filtering, the CLS dataset exhibits residual meridional striping due to satellite sampling artifacts (Auger et al., 2022). This

208 pattern is significantly suppressed with a 150 km Gaussian filter. Between the filtered CLS-derived w_e (150 km) and CPOM-

209 derived w_e, the correlation coefficients improving markedly from 0.77 (no filter) to over 0.95 (p < 0.05).

210

211
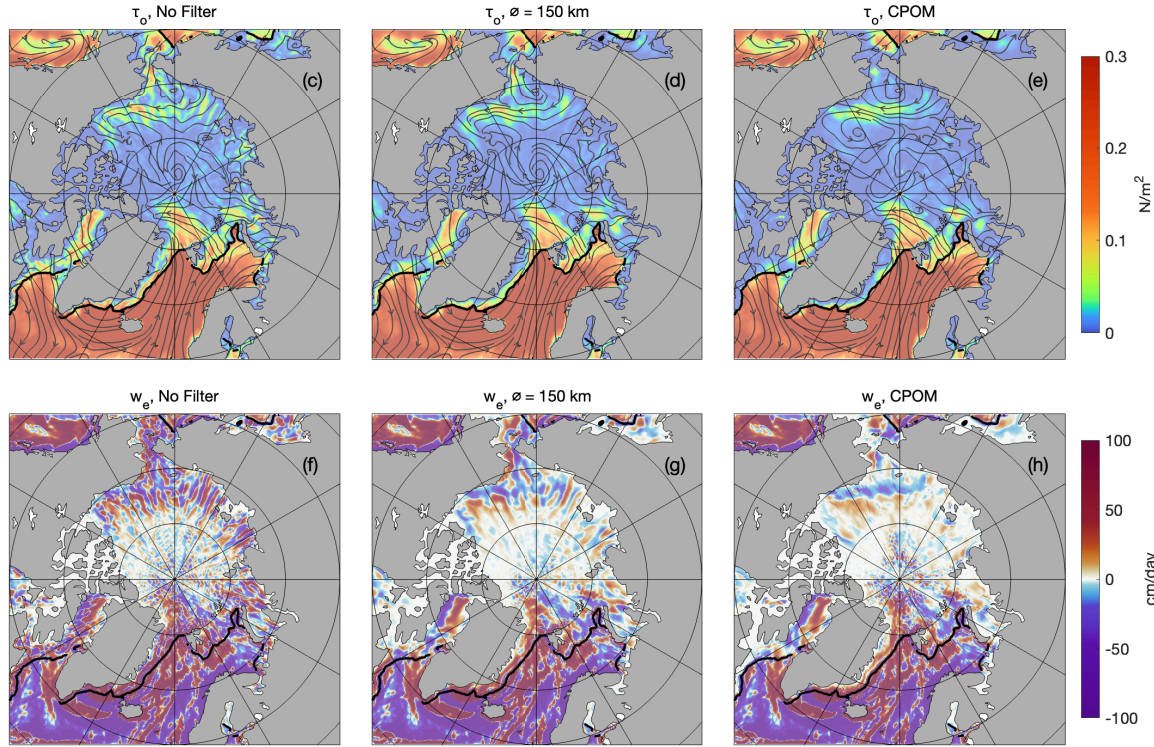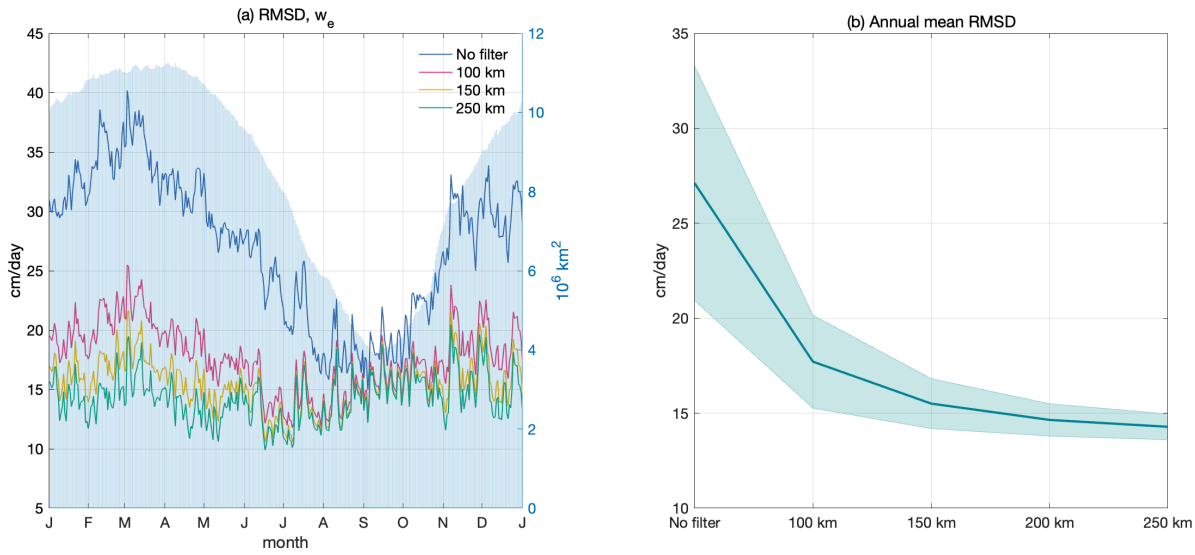
Figure 3: Area-averaged ocean-surface stress τ_o and vertical Ekman velocity w_e regarding Gaussian filter setting. (a) Annual cycle
of root mean squared deviation (RMSD) of w_e over 2011. Blue shades show total ice-cover areas (right axis). (b) Annual mean RMSD
of w_e with shading indicating one standard deviation over a year. (c) Snapshot of τ_o with unfiltered CLS (3/15/2011). (d) Same as c
but with 150 km Gaussian filter. (e) Same as c but with CPOM. (f-h) Same as (c-e) but for w_e. Streamlines in (c-e) show the direction
of τ_o. Black contours in (c-h) mark the 15% ice concentration on 3/15/2011.

217

3 Results and Regional Statistics

3.1 Arctic Ocean

In this section, we provide a concise overview of the surface stress and the corresponding Ekman velocity fields. Figure 4a shows the time-averaged ocean-surface stress (τ_o) field across the Arctic for 2011–2018. The highest τ_o appears in the ice-free Nordic Seas, where strong wind-ocean interactions drive surface stress exceeding 0.3 N/m². In contrast, sea ice reduces momentum transfer and lower the τ_o in ice-covered regions. In the Seasonal Ice Zone (SIZ), marked by the March and September sea ice boundaries, τ_o typically remains below 0.05 N/m². Within the Perennial Ice Zone (PIZ), bounded by the September sea ice boundary, it drops further to below 0.02 N/m².

The seasonal cycle of τ_o is the dominant temporal variability across the Arctic (Stroeve and Notz, 2018). The standard deviation (STD) shows a spatial distribution similar to the time-averaged τ_o (Figure 4b), with high variability (>0.1 N/m²) in ice-free regions like the Nordic Seas. Variability is significantly suppressed in the SIZ and PIZ, with values below 0.02 N/m² and 0.01 N/m², respectively. The coefficient of determination (R^2, here is calculated as the proportion of variance explained by the seasonal cycle, i.e., $R^2 = 1 - \frac{\sum_i (y_i - y_{seasonal})^2}{\sum_i (y_i - \bar{y})^2}$) shows that in open-ocean regions, 40–60% of variance is explained by seasonal variability (Figure 4c). In ice-covered areas, this ratio drops to less than 30%.

The time-mean Ekman pumping rate (w_e), alongside its STD and R^2 patterns are given in Figure 4d-f. Strong upwelling (>50 cm/day) is observed in the Nordic Seas, while strong downwelling (<-10 cm/day) occurs in the Beaufort and Chukchi Seas. The spatial pattern of STD w_e is similar to that of τ_o (Figure 4e). Seasonal variability ranges from 10–20 cm/day in ice-free regions, 4–6 cm/day in SIZ, and falls below 4 cm/day in the PIZ. Seasonal variability accounts for up to 60% of w_e variance south of the Denmark Strait, but in other regions, including both ice-covered and ice-free zones, it typically explains 10–30%.
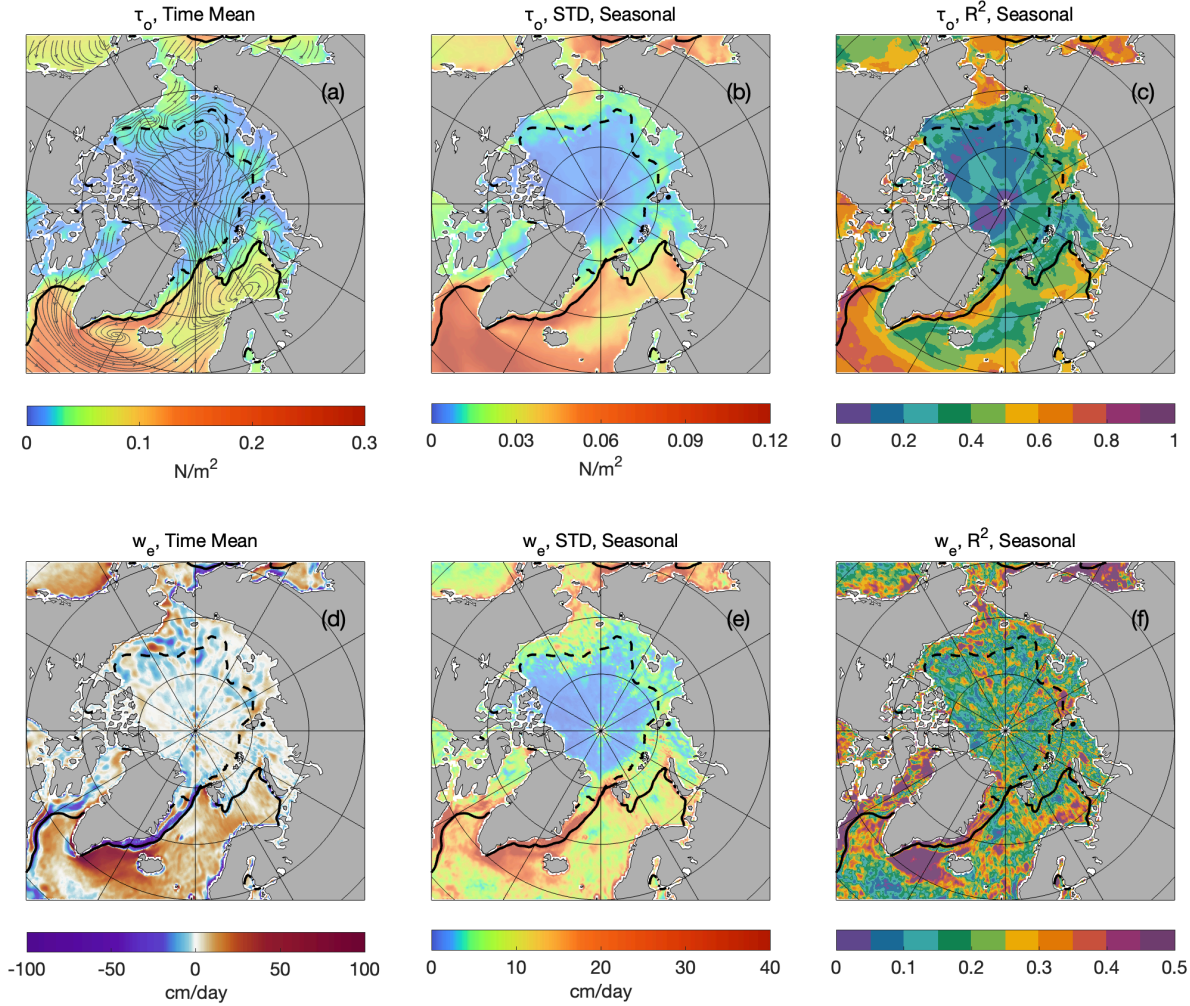
Figure 4: Mean and variability of ocean-surface stress τ_o and Ekman pumping rate w_e (positive indicates upwelling, negative indicates downwelling) in the Arctic region over 2011-2018. (a) Mean τ_o, with streamlines indicating the direction of stress. (b) Standard deviation of τ_o seasonal variability. (c) R^2, representing τ_o variance explained by seasonal variability. (d-f) Same as (a-c) but for w_e. Streamlines in (a) show the direction of τ_o. The solid and dashed black lines represent the March and September sea ice boundaries, respectively, defined by 15% sea ice concentration averaged over 2011-2018.

The seasonal cycle of area-averaged wind-ocean surface stress (τ_{aw}) is marked by strong values in winter, peaking around 0.4 N/m² and much weaker values in summer, dropping below 0.05 N/m² (Figure 5a). This variation corresponds to the seasonal retreat of sea ice and the associated expansion of open ocean during summer months.

In ice-covered regions, the seasonal cycle of ice-ocean surface stress (τ_{iw}) is similar to that of τ_{aw}, though with significantly lower magnitudes (Figure 5c). The seasonal peak of τ_{iw} is slightly higher in 2018 than 2013, increasing from 0.010 N/m² to nearly 0.018 N/m².

251 In ice-free regions, the average pumping rate $w_{e,aw}$ peaks during winter upwelling, reaching around 30 cm/day, and transitions

252 to weak downwelling during the summer (Figure 5e). Annual variation in winter maximum upwelling rate is evident, with a

253 notable decline to 10 cm/day by late 2018 (Figure 5f). In contrast, in ice-covered regions, $w_{e,iw}$ is predominantly negative

254 (Figure 5g), although occasional summer upwelling events occur on daily scales. Notably, the winter downwelling rate has

255 decreased from approximately -8 cm/day in 2013–2014 to about -4 cm/day by 2017.

256

257

264

3.2 Southern Ocean

266 The spatial distribution of the time-mean τ_o in the Antarctic region is shown in Figure 6a. τ_o exhibits a prominent circumpolar

267 pattern. In ice-free regions, τ_o typically ranges from 0.2 to 0.3 N/m². In the SIZ, τ_o decreases significantly, falling to 0.04–

268 0.06 N/m², with strong regional variability.

269 The STD of τ_o seasonal variability is evidently strong near the September sea ice boundary, exceeding 0.1 N/m², particularly

270 between 0-90°E (Figure 6b). Moving northward into subpolar open-ocean, the STD gradually declines to approximately 0.04

271 N/m². Within the SIZ, seasonal variability diminishes further, typically ranging from 0.02 to 0.04 N/m². In the PIZ, it drops

272 below 0.02 N/m². The R² shows that in regions such as the Indian Ocean and southeast Pacific, seasonality explains over 50%

273 of the total variance, while in other areas, this proportion ranges from 20% to 40% (Figure 6c).

274 The spatial structure of the time-mean w_e reveals widespread upwelling south of 50°S (Figure 6d), extending nearly all the

275 way to the coast of Antarctica. In contrast to the Arctic, where strong ice-ocean coupling leads to clear transitions between

276 upwelling and downwelling across ice boundaries, the Southern Ocean does not exhibit this distinct pattern. Downwelling is

277 generally found around 55°S and farther north, or more narrowly along the Antarctic coastline.

278 The STD pattern of seasonal variability in w_e is relatively consistent across the Southern Ocean (Figure 6e), regardless of sea-

279 ice coverage, with an average value of approximately 10 cm/day. Higher variability, reaching up to 20 cm/day, occurs only

280 near the September ice boundary and is very localized. The R² pattern is also relatively homogeneous, with most areas showing

281 seasonal variability accounting for about 30% of the variance. Along the east coast of Antarctica, the seasonal cycle explains

282 more than 50% of the variance.

283

284
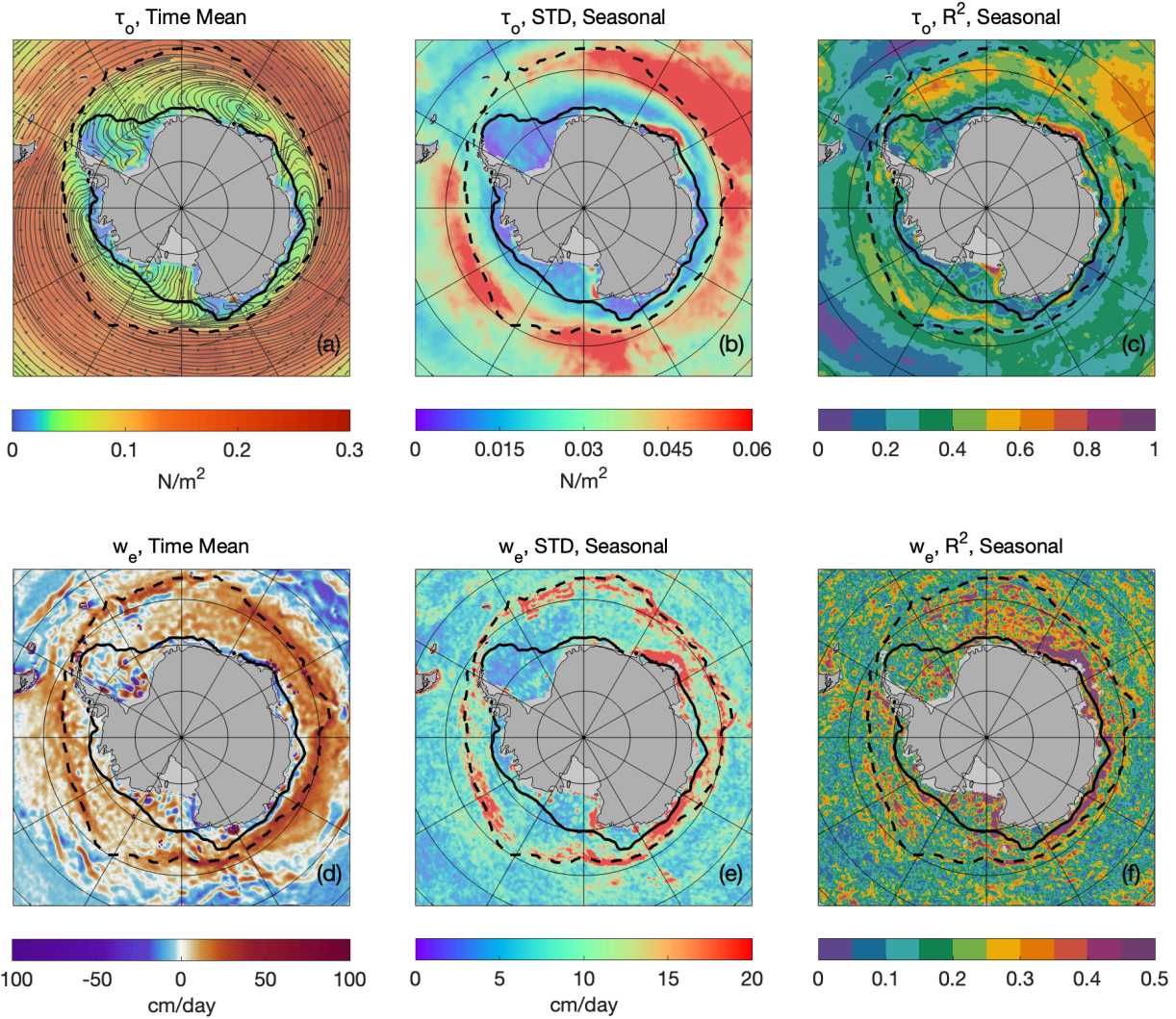
Figure 6: Mean and variability of ocean-surface stress τ_o and Ekman pumping rate w_e (positive indicates upwelling, negative indicates downwelling) in the Antarctic region over 2013-2018. (a) Mean τ_o, with streamlines indicating the direction of stress. (b) Standard deviation of τ_o seasonal variability. (c) R^2, representing τ_o variance explained by seasonal variability. (d-f) Same as (a-c) but for w_e. Streamlines in (a) show the direction of τ_o. The solid and dashed black lines represent the March and September sea ice boundaries, respectively, defined by 15% sea ice concentration averaged over 2013-2018.

The seasonal cycle and time series of area-averaged air-water stress τ_{aw} in the Antarctic are shown in Figures 7a and 7b. In ice-free regions of the Antarctic, the average τ_{aw} peaks in August at 0.36 N/m² and reaches its minimum in January at 0.13 N/m². Annual variability is relatively small, ranging between 0.022 and 0.026 N/m², with a notable positive anomaly in 2015, when the annual mean briefly increased to 0.028 N/m².

In ice-covered regions, ice-water stress τ_{iw} shows a delayed seasonal cycle compared to τ_{aw} and peaks in September (Figure 7c). It is approximately one-fifth to one-half of τ_{aw}, ranging between 0.02 N/m² and 0.08 N/m². The seasonal pattern is

297   asymmetrical and aligns with the seasonal cycle of sea ice coverage (Eayrs et al., 2019). Similar to the Arctic, the area-averaged

298   summer minima of τ_{iw} is slightly higher in 2018 compared to 2013, increasing from 0.010 N/m² in to 0.022 N/m².

299   The seasonal cycle of open-ocean Ekman pumping rate $w_{e,aw}$ is relatively weak (Figure 7e), with higher values in winter (12

300   cm/day) and lower values in summer (5 cm/day). The absence of a distinct seasonal signal is likely due to the weaker seasonal

301   cycle observed in 2017 and 2018 (Figure 7f). The annual mean varies narrowly between 7 and 9 cm/day.

302   In ice-covered regions, $w_{e,iw}$ is mostly positive throughout the year, with a brief downwelling period between January and

303   April. A shift toward stronger downwelling occurs in February, with mean values decreasing from -2 cm/day in 2013 to nearly

304   -10 cm/day by 2017. A notable anomaly occurred in 2015 when the annual mean rose sharply from 2 cm/day to 4 cm/day.

305
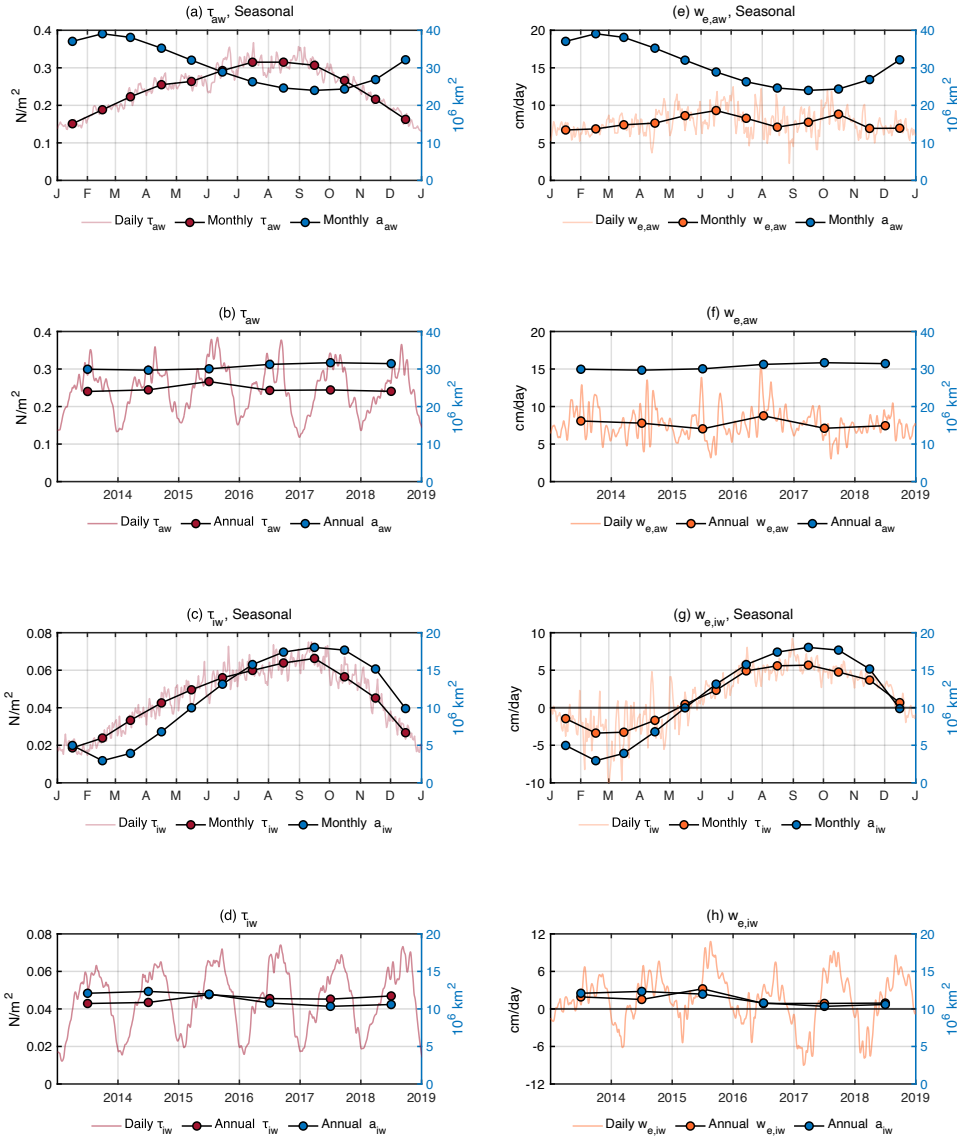
306

Figure 7: Timeseries and seasonal cycle of area-averaged surface stress τ_o (red) and Ekman pumping rate w_e (orange, positive indicates upwelling, negative indicates downwelling) for the Antarctic region. Total areas a of the corresponding areal coverage are also plotted in blue. Variables are subscripted aw when averaged/summed over ice-free open ocean, and are subscripted iw when averaged/summed over ice-covered open ocean. Annual and monthly means are shown as dots in all panels. (a) Seasonal cycle of τ_{aw} over the ice-free open ocean. (b) Timeseries of τ_{aw} from 2013-2018. (c) Seasonal cycle of τ_{iw} over the ice-covered ocean. (d) Timeseries of τ_{iw} from 2013-2018. (e-h) same as (a-d) but for w_e.

4 Uncertainty and Data Quality Assessment

4.1 Sensitivity Analysis of Ice-Water Drag Coefficient and uncertainty estimate

The ice-water drag coefficient, $C_{D,iw}$ is often assumed to be constant across time and space due to the scarcity of direct observations that capture its spatiotemporal variability. However, $C_{D,iw}$ can vary significantly depending on environmental conditions such as wind and wave dynamics, ice roughness, sea ice concentration, and surface morphology (Lüpkes et al., 2012; Lüpkes and Birnbaum, 2005; Cole & Stadler, 2019). Reported values for $C_{D,iw}$ range from 0.7 to over 10.0×10^{-3} (Overland, 1985; Guest and Davidson, 1987, 1991; McPhee, 2008; Cole et al., 2014), with some extreme cases reaching magnitudes on the order of 10.0×10^{-1} (Kawaguchi et al., 2024).

Commonly, a representative value of 5.5×10^{-3} has been widely adopted as a pragmatic approximation by the scientific community (Guest and Davidson, 1987; Anderson, 1987). However, this approximation may overlook important spatial and temporal variations in $C_{D,iw}$, highlighting the need for ongoing efforts to improve observations and refine its parameterization. To evaluate the sensitivity of estimated τ_o to the variations in $C_{D,iw}$, two sets of experiments are conducted for 2011: one with fixed $C_{D,iw}$ values ranging from 1.0×10^{-3} to 10.0×10^{-3}, and another using a randomized weighting map, dynamically varying $C_{D,iw}$ between between order of 10^{-3} and 10^{-2} on a daily basis at each grid cell.

The amplitude of τ_o scales proportionally with $C_{D,iw}$, as implied from Eq. 2 (Figure 8a). For fixed coefficients, the summer mean τ_o increases from 0.003 N/m² at $C_{D,iw} = 1.0 \times 10^{-3}$, to 0.015 N/m² at $C_{D,iw} = 10.0 \times 10^{-3}$, while winter means rise from 0.012 N/m² to 0.053 N/m². Results from the random-weighted $C_{D,iw}$ experiment closely follows the fixed cases of $C_{D,iw} = 5.0$-6.0×10^{-3}. Similarly, the annual mean τ_o and its standard deviation increase proportionally with $C_{D,iw}$ (Figure 8b), quadrupling the annual mean and raising the standard deviation from 0.003 N/m² to 0.017 N/m² as $C_{D,iw}$ increases.

Figures 8c–h show the spatial distribution of τ_o and w_e in response to varying $C_{D,iw}$. Under low $C_{D,iw}$ circumstances, momentum transfer between ice and ocean is reduced, leaving small scale variability indistinct particularly in the central Arctic. As $C_{D,iw}$ increases, regions with high surface stress intensify, particularly in areas like Baffin Bay, the Chukchi Sea, and north of Fram Strait.

At $C_{D,iw} = 1.0 \times 10^{-3}$, the Ekman pumping rate in regions like the Fram Strait barely reach ±8 cm/day, whereas at $C_{D,iw} = 10.0 \times 10^{-3}$, it exceeds ±30 cm/day, with strong contrasting upwelling and downwelling patterns. additionally, while the random-

339 weighted $C_{D,iw}$ experiment introduces spatial noise, the broader spatial structures of both τ_o and w_e remain consistent with
340 fixed-coefficient runs.

341

342
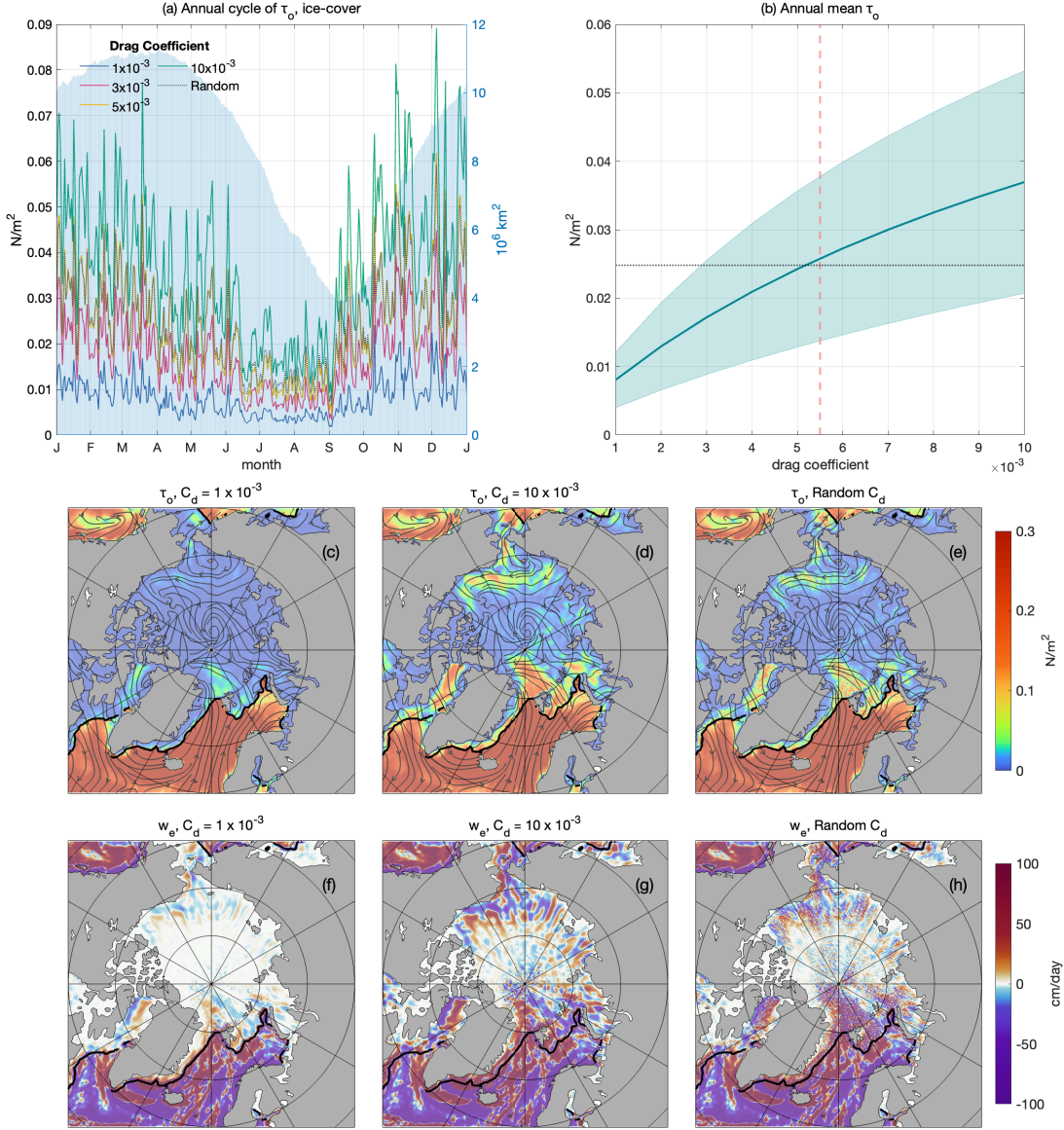
Figure 8: Area-averaged ocean-surface stress τ_o and Ekman pumping rate w_e regarding different $C_{D,iw}$. (a) annual cycle of τ_o of 2011, area-averaged over the sea ice-cover region. Blue areas show total ice-cover areas (right axis); (b) annual mean of τ_o with shading indicating one standard deviation over a year. Red dashed line marks $C_{D,iw} = 5.5 \times 10^{-3}$, black dotted line shows the annual mean of random $C_{D,iw}$ experiment. (c) Snapshot of τ_o with $C_{D,iw} = 1.0 \times 10^{-3}$ (3/15/2011). (d) Same as c but with $C_{D,iw} = 10.0 \times 10^{-3}$. (e) Same as c but with random $C_{D,iw}$. (f-h) Same as (c-e) but for w_e. Streamlines in (c-e) show the direction of τ_o. Black contours in (c-h) mark the 15% ice concentration on 3/15/2011.

350 The final estimated uncertainty ε_{iw}, in the ice-water stress τ_{iw} is quantified daily through the integration of standard errors

351 from sensitivity analyses of $C_{D,iw}$ and spatial Gaussian filter tests. Both filter tests and $C_{D,iw}$ tests are extended to the full

352 analysis period: eight years (2011–2018) for the Arctic and six years (2013–2018) for the Antarctic. Using the root-sum-square

353 method, the combined uncertainty is expressed as:

$$354 \quad \varepsilon_{iw} = \sqrt{(\varepsilon_{iw,F})^2 + (\varepsilon_{iw,C})^2} = \sqrt{(\frac{\sigma_F}{\sqrt{N_1}})^2 + (\frac{\sigma_C}{\sqrt{N_2}})^2} \tag{7}$$

355 where σ_F is the standard deviation of τ_{iw} from different Gaussian filter settings, and σ_C represents the standard deviation of

356 τ_{iw} from sensitivity analysis on varying $C_{D,iw}$. The terms N_1 and N_2 denote the number of runs performed in each sensitivity

357 analysis. This estimate assumes independence between $C_{D,iw}$ and geostrophic fields (which were spatially filtered), with

358 perturbations of comparable amplitude between the two sets of sensitivity analysis.

359 Figure 9 shows the spatial distributions of relative uncertainty (ε_{iw} to τ_{iw}) for the Arctic (March 15, 2013) and the Southern

360 Ocean (September 15, 2013) during winter season. Overall, spatial filtering produces scattered patterns (Figures 9a–9d), while

361 varying ice-water drag coefficient yield smoother distributions (Figures 9e–9h). Median uncertainties are comparable between

362 the two sets of experiments, ranging from 14–18% in the Arctic to 22–25% in the Antarctic. The greater uncertainties in the

363 Antarctic reflect higher local stress variability and increased sensitivity to parameter changes, which also manifests as the

364 higher uncertainties observed in winter compared to summer (Figures 3 and 8).

365 In the Arctic, combined uncertainties for zonal surface stress (τ_x) typically range from 10–20%, while locally it could exceed

366 100% along dynamic regions such as the Fram Strait and Beaufort Sea. Meridional stress (τ_y) exhibits similar spatial

367 distributions, but with higher uncertainties near the Mendeleev Ridge. Median uncertainty levels for both zonal and meridional

368 components are below 20%.

369 Conversely, Antarctic uncertainties are substantially higher, with median values around 40%. The highest uncertainties (>60%)

370 are concentrated near the sea ice boundary, particularly in the eastern Weddell and Ross Seas. Regional hotspots include the

371 Antarctic Peninsula and west of Ross Sea for τ_x, and Enderby Land and the Amundsen Sea for τ_y.

373
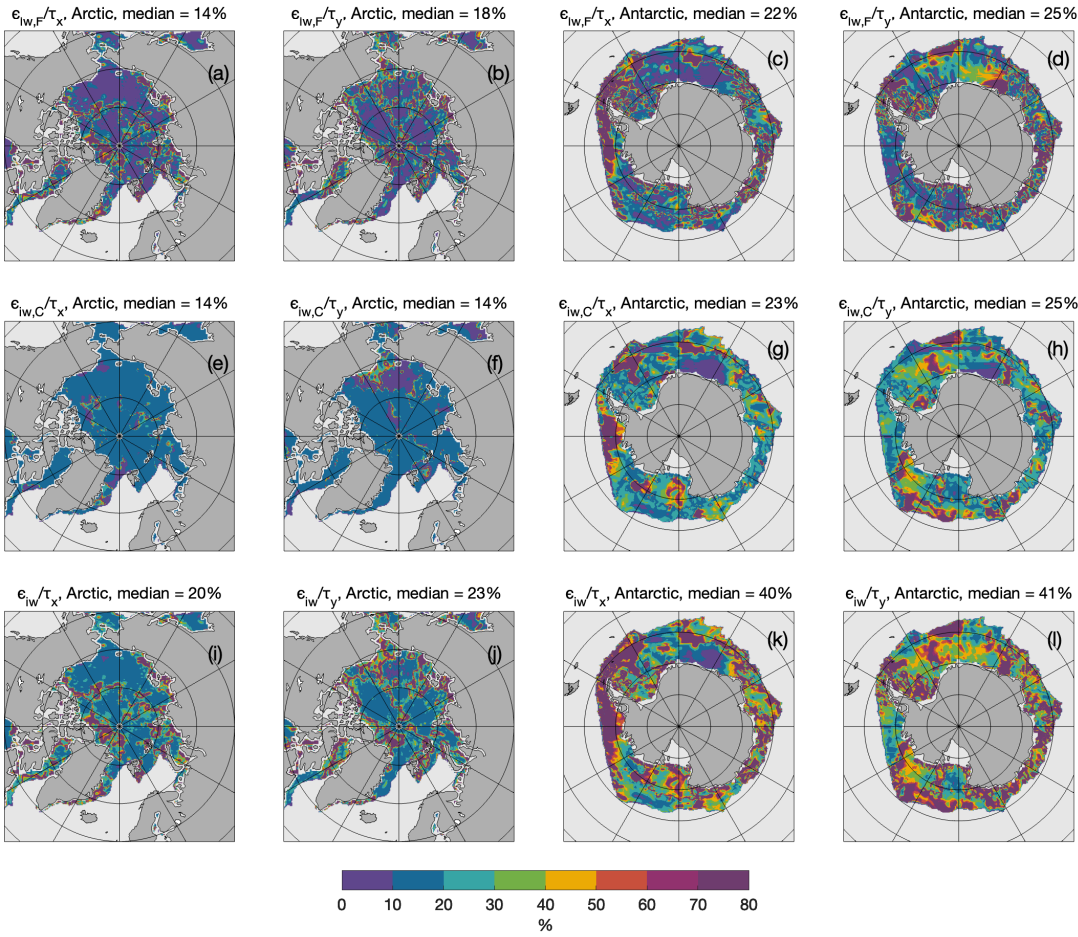
Figure 9: Estimated uncertainty fields for zonal and meridional ice-water surface stress, expressed as a ratio to the estimated ice-water surface stress in the Arctic (3/15/2013) and Southern Ocean (9/15/2013). (a) standard error introduced by Gaussian filter in the Arctic, zonal direction; (b) error from filter in the Arctic, meridional direction; (c-d) same as (a-b) but for the Antarctic; (e-h) same as (a-d) but for standard error in ice-water drag coefficient $C_{D,iw}$; (i-l) same as (a-d) but for the combined uncertainty.

378

379 In addition to the sensitivity analyses presented for drag coefficient magnitudes and spatial filtering, several other sources of

380 uncertainty may influence the accuracy of the derived surface stress fields. First, uncertainties in the atmospheric reanalysis

381 products used as forcing data—particularly in wind speed and direction over sea ice—can propagate directly into surface stress

382 estimates. Prior studies have shown that different ice motion products can yield differences of at least 20–30% in polar regions

383 due to discrepancies in boundary-layer representation, data assimilation techniques, and satellite retrieval biases (Sumata et

384 al., 2014; Wang et al., 2022). These differences are especially pronounced in the marginal ice zone, where sharp gradients in

385 atmospheric and surface properties are common (Wang et al., 2021; Boutin et al., 2020).

386

Second, the role of ocean and atmospheric stratification is not explicitly resolved in our parameterization, yet it can significantly affect stress transmission through the ice–ocean interface. Observational and modeling studies (Lüpkes & Gryanik, 2015; Lüpkes et al., 2012; Brenner et al., 2021) have shown that stability conditions in the atmospheric boundary layer modulate drag coefficients by altering turbulence and momentum fluxes—especially under stable stratification, common in winter Arctic conditions. Likewise, vertical stratification in the upper ocean can modify Ekman layer dynamics and the effective depth over which stress-induced velocities operate, introducing further uncertainty in estimates of vertical transport (Meneghello et al., 2018; Zhong et al., 2018).

Third, the spatial and temporal scales over which stresses are calculated can introduce methodological uncertainty. Coarse averaging may obscure high-frequency processes such as synoptic wind events, inertial motions, or mesoscale eddies, while finer-scale estimates risk amplifying local noise or aliasing undersampled variability (Timmermans et al., 2008; Manucharyan & Thompson, 2017; Alberello et al., 2020). This is particularly relevant in the marginal ice zone, where surface properties evolve rapidly. A more detailed analysis of scale effects and filtering sensitivity is presented in the following section.

Together, these factors point to the need for caution when interpreting surface stress magnitudes or derived quantities like Ekman pumping, particularly when used to constrain physical budgets or force ocean models. Future work should prioritize uncertainty quantification through ensemble reanalysis comparisons, the inclusion of stratification effects in drag parameterizations, and adaptive filtering techniques that respond to local dynamical conditions.

4.2 Validation with ITP Observations

Since surface stress is not usually directly measured, assessing the performance of our analysis is challenging. To address this, we revisit the assumption that surface velocity comprises both Ekman and geostrophic components, as described in Eq. (2). The geostrophic velocity (U_g) is derived from the dataset provided by Prandi et al. (2021), while the Ekman velocity component (U_e) can be easily calculated from the ocean-surface stress using Eq. (4).

This assumption provides a first-order approximation of surface velocity, and neglects other processes, such as ageostrophic motions, vertical shear, and submesoscale dynamics, which may introduce additional uncertainties. To robustly validate satellite-derived ocean surface stress estimates, we compared the derived surface velocity, i.e., sum of U_g and U_e, with in situ measurements from Ice-Tethered Profilers (ITPs, Krishfield et al., 2008; Toole et al., 2011; http://www.whoi.edu/itp). In particular, several ITPs that equipped velocity sensors (ITP-V, Williams et al., 2010) are used. To align the temporal resolution of the datasets, we processed the ITP data by computing daily and weekly means, facilitating direct comparisons with daily satellite products. This approach avoids the uncertainties associated with interpolating satellite data to match the higher-frequency ITP profiles, which could introduce significant errors due to the under-sampling nature of satellite observations.

Despite this temporal alignment, inherent limitations persist due to spatial and temporal sampling discrepancies. ITPs provide high-resolution vertical profiles at specific locations, capturing fine-scale and transient oceanic features. In contrast, satellite observations offer broader spatial coverage but may not resolve such fine-scale variability, especially in polar regions where

data gaps are common due to persistent cloud cover and sea ice. These differences can lead to reduced correlation and increased bias in validation statistics, as observed in previous studies comparing satellite-derived sea surface salinity products with in situ observations (Thouvenin-Masson et al., 2022; Boutin et al., 2016; Vinogradova & Ponte, 2013).

It is important to note that this comparison does not serve as a definitive validation of the absolute accuracy of our stress estimates. Instead, it assesses whether the foundational assumptions underpinning our analysis sufficiently represent the complex dynamics of the Arctic Ocean.

We use velocity data collected from five ITP-V missions deployed on multiyear sea ice in the Canada Basin between 2011 and 2019 (Figure 10; Table 2). Observations from ITP-77, ITP-78, and ITP-79 are truncated to exclude periods with significant data gaps and drifts near the end of their deployments.

The five ITP-Vs are categorized into two groups based on deployment timing and drift trajectories. ITP-70 and ITP-80 were deployed during summer, operated for ~300 days, and primarily drifted between 75–80°N. In contrast, ITP-77, ITP-78, and ITP-79, deployed in March 2014, operated for less than 200 days and followed more constrained east-to-west trajectories between 73–75°N.

Table 2: Details of the ITP-V records

Unit ID	Start		Last		# of Days	# of Profiles
	Position	Date	Position	Date		
ITP-70	76.81°N 138.89°W	8/26/2013	77.11°N 156.51°W	7/15/2014	324	3713
ITP-77	73.37°N 134.99°W	3/11/2014	75.89°N 158.50°W	10/2/2014	206 (153[*])	2367 (1800[*])
ITP-78	74.36°N 135.14°W	3/12/2014	74.08°N 145.43°W	8/6/2014	148 (130[*])	1694 (1500[*])
ITP-79	75.38°N 136.50°W	3/22/2014	75.02°N 148.37°W	9/30/2014	193 (143[*])	1694 (1636[*])
ITP-80	77.36°N 146.15°W	8/14/2014	75.68°N 151.79°W	5/24/2015	284	3260

[*] Data towards the end of the series exhibits quality issues that necessitate truncation.

436
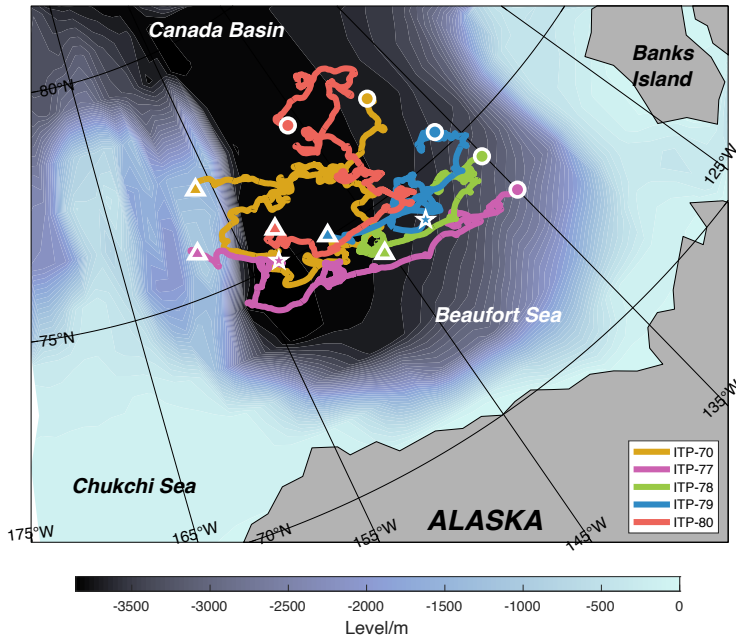
Figure 10: ITP-V drift paths in the Arctic Ocean (colored curves). The deployment locations are marked by circles, latest locations by triangles, and the cutoff locations for ITP-77 and ITP-79 by stars.

439

To account for temporal sampling differences and mitigate aliasing from high-frequency variability, the sub-daily ITP-V velocity data are first averaged to daily means before comparison with the satellite-derived velocity field (U_g+U_e). The corresponding satellite values are then extracted at the nearest grid point along each ITP track (Figure 11). This approach reduces mismatch due to subsampling in the satellite product and ensures a more consistent temporal basis for comparison. Along the path of ITP-70 and ITP-80, satellite-derived ocean surface velocities exhibit moderate agreement with in situ observations, particularly in capturing high-frequency variability. In contrast, comparisons with ITP-77, ITP-78, and ITP-79 reveal weaker correspondence, most notably in the zonal velocity components. For the meridional component, ITP-77 shows relatively better alignment during the initial ~100-day period until mid-July.

448

449
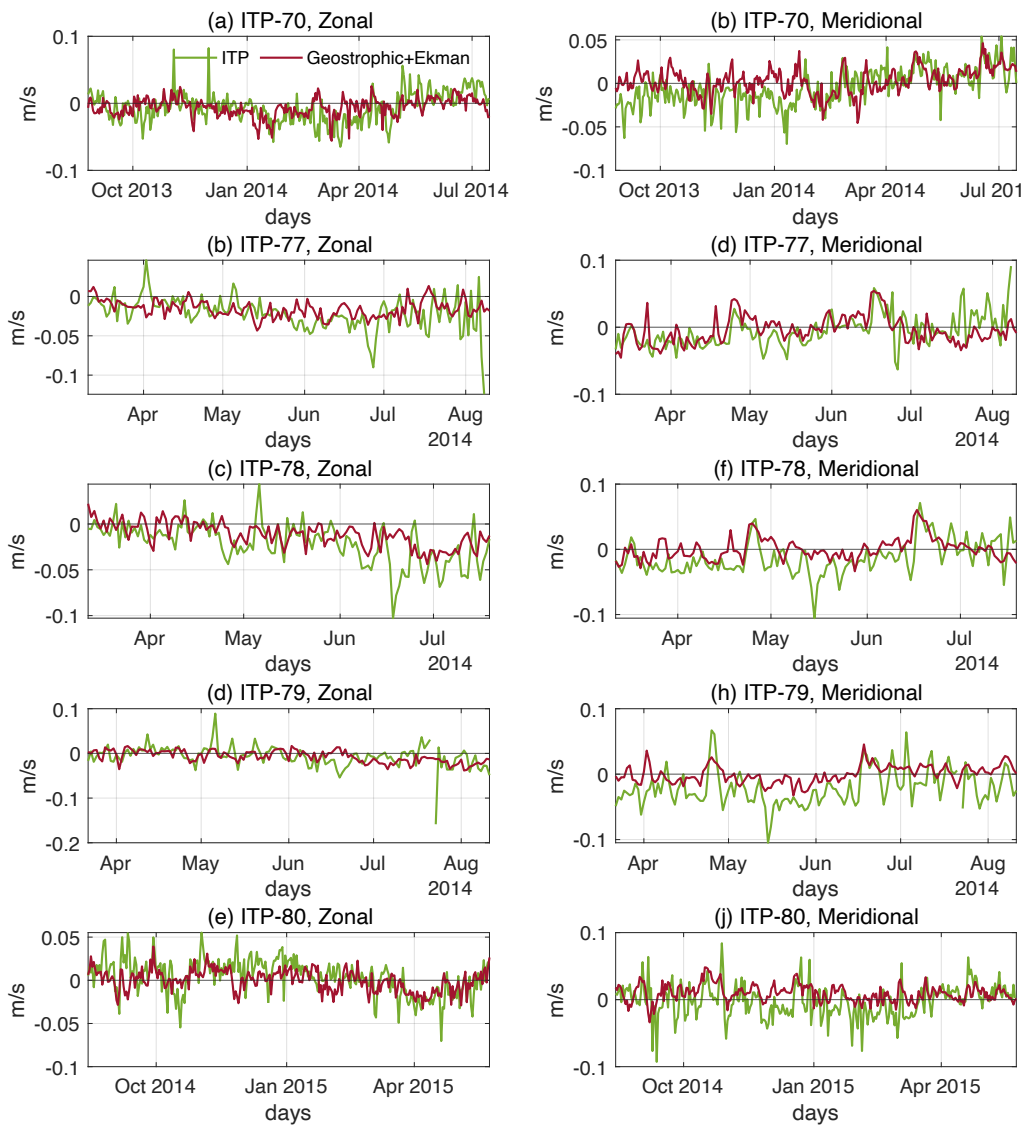
Figure 11: Daily mean timeseries of zonal and meridional surface velocity. (a) Zonal velocity along ITP-70 paths. (b) Zonal velocity along ITP-77 paths. (c) Zonal velocity along ITP-78 paths. (d) Zonal velocity along ITP-79 paths. (e) Zonal velocity along ITP-80 paths. (f-j) same as (a-e) but for meridional velocity. Green curves represent velocity data retrieved from ITPs. Red curves are collocated obtained from the satellite-derived velocity fields, i.e., geostrophic plus Ekman velocity.

454

Figure 12 presents the comparison of satellite-derived surface velocity components against collocated ITP-V observations for the ITP-70 (panels a,b) and ITP-80 (panels c,d) paths. For ITP-70, the zonal component yields a Pearson correlation of $r = 0.31$ and standard deviation of 0.022 m s^{-1}, while the meridional component gives $r = 0.42$ and STD = 0.020 m s^{-1}. ITP-80 exhibits slightly stronger zonal agreement ($r = 0.43$) but weaker meridional agreement ($r = 0.34$). In both deployments, scatter

459   markedly decreases for observations taken after ~200 days (warm colors), accompanied with the predominantly northward
460   drift of ITP-70 and westward drift of ITP-80 seen in Figure 10.

461
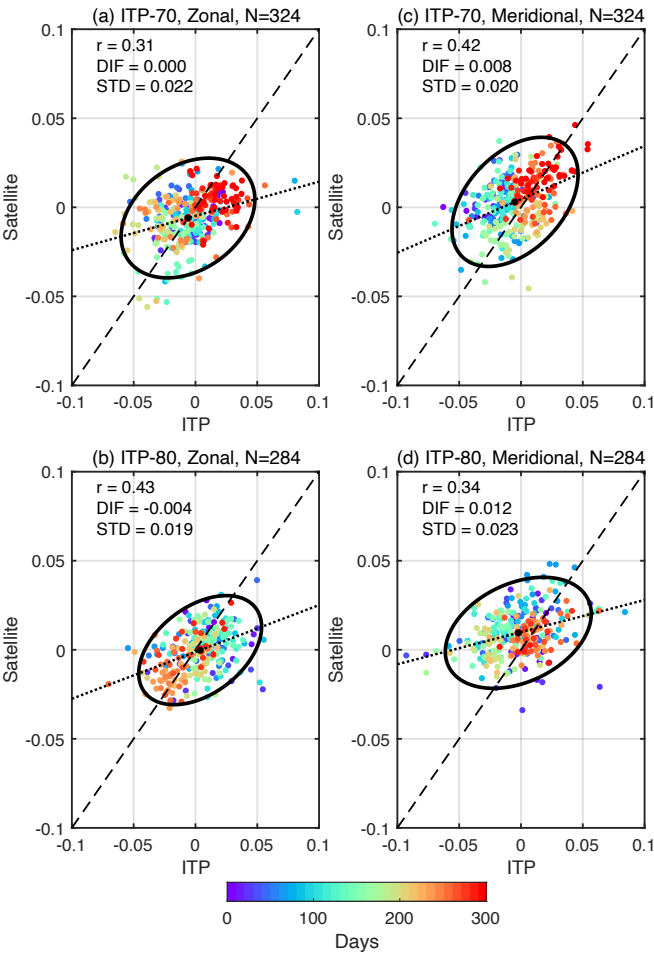
462
463   **Figure 12: Scatterplots of collocated surface velocity pairs for ITPs with data spanning more than 200 days (unit: m/s). (a) Zonal**
464   **velocity along ITP-70 paths. (b) Zonal velocity along ITP-80 paths. (c-d) Same as (a-b) but for meridional velocity. The total number**
465   **of days (N) is given. Correlation coefficients, mean differences (DIF), and standard deviations (STD) of the differences between**
466   **satellite-derived velocity and ITP observations are also displayed. 95% confidence ellipse (black contour), linear fitting (black dotted**
467   **line) are also given in each panel.**

468

469   By contrast, Figure 13 summarizes the additional ITP observational periods (panels a–f), where correlation coefficients span
470    $r = 0.07$–0.56, and STD = 0.021–0.025 m s^{-1}. One component reaches a moderate correlation ($r = 0.56$), while most remain
471   weak ($r < 0.40$), and no coherent temporal clustering is apparent. Across all deployments, satellite-derived velocities exhibit a
472   slight northward bias and tend to underestimate ITP-measured surface speeds beyond 100 days post-release.

473

474
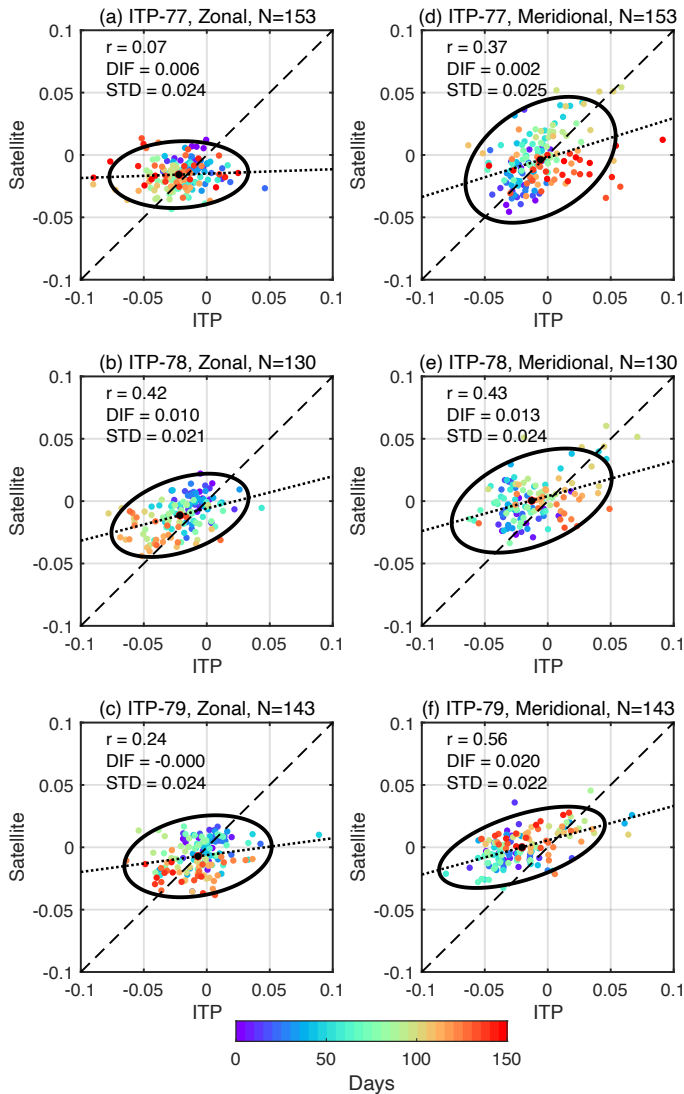
Figure 13: Scatterplots of collocated surface velocity pairs for ITPs with data spanning less than 200 days (unit: m/s). (a) Zonal velocity along ITP-77 paths. (b) Zonal velocity along ITP-78 paths. (c) Zonal velocity along ITP-79 paths. (d-f) Same as (a-c) but for meridional velocity. The total number of days (N) is given. Correlation coefficients, mean differences (DIF), and standard deviations (STD) of the differences between satellite-derived velocity and ITP observations are displayed. 95% confidence ellipse (black contour), linear fitting (black dotted line) are also given in each panel.

480

Table 2 and Figure 14 provide a comprehensive comparison between satellite-derived surface velocity estimates and in situ velocity measurements obtained from ITP-V across five deployments. The analysis includes both the zonal (east–west) and meridional (north–south) velocity components and considers statistics derived from both daily and weekly averaged timeseries. A consistent northward bias is evident in the satellite-derived velocities across most ITP paths. While the mean zonal velocities are generally in close agreement between satellite and ITP-V data—for instance, at ITP-70 both sources report a mean of –

486 0.006 m/s—some deployments exhibit a more pronounced bias. ITP-77 and ITP-78, in particular, show a noticeable eastward
487 offset, with satellite-derived zonal velocities being more positive than the ITP-V counterparts by approximately 0.005–0.01
488 m/s. The meridional component aligns more closely overall, but satellite velocities still tend to be more northward. These
489 biases are evident in the top-left panel of Figure 14, where most points lie above the 1:1 line, especially in the meridional
490 direction.

491 In addition to the bias, satellite-derived velocities systematically exhibit reduced variability compared to ITP-V observations.
492 Across all deployments and components, the STD of satellite velocity is consistently lower than that observed in the ITP-V
493 data. For example, while the average zonal STD in the ITP data is around 0.022 m/s, the corresponding satellite value is
494 approximately 0.011 m/s. The top-right panel of Figure 14 illustrates this discrepancy clearly: all data points fall below the 1:1
495 line, indicating that satellite products underestimate temporal variability. This reduced variability likely reflects the filtering
496 and smoothing inherent in satellite altimetry products, which are designed to represent large-scale geostrophic flows and may
497 not fully resolve the higher-frequency or smaller-scale fluctuations captured by the ITP instruments.

498 Despite these limitations, satellite-derived velocity fields are able to explain a substantial portion of the observed variance in
499 the ITP-V measurements on daily mean scale. The coefficient of determination (R^2) values indicate that, on average, satellite
500 products account for about 50% of the variability in the daily data. This explanatory power increases substantially when the
501 analysis is performed on weekly averaged time series, with R^2 reaching as high as 0.77 for the zonal component at ITP-78 and
502 0.60 for the meridional component at ITP-79. These results suggest that, although satellite estimates smooth out finer-scale
503 variability, they capture the dominant patterns in large-scale motion effectively. However, the correlation coefficients between
504 satellite and ITP-V velocities are more modest, typically ranging from 0.3 to 0.4 in the daily records. With weekly averaging,
505 these correlations improve significantly, sometimes by more than 0.2, as illustrated in the bottom-left panel of Figure 14. This
506 panel shows weekly-averaged points clustering nearer to or above the diagonal, particularly for ITP-78 and ITP-79, while daily
507 correlations tend to remain lower and more scattered.

508 The performance of the satellite velocity estimates varies by deployment. ITP-78 and ITP-79 demonstrate the strongest
509 agreement. For example, ITP-78's zonal component yields correlation coefficients of 0.42 for daily data and 0.78 for weekly
510 data, with R^2 values of 0.32 and 0.77, respectively. Similarly, ITP-79's meridional component shows a daily correlation of
511 0.56 and a weekly correlation of 0.76, with corresponding R^2 values of 0.47 and 0.60. These high values underscore the ability
512 of satellite altimetry to capture meaningful geophysical signals under favorable conditions. Conversely, performance is notably
513 weaker at ITP-77, where the zonal velocity component yields a daily correlation of only 0.07 and a weekly correlation of 0.31,
514 suggesting a diminished ability of satellite products to resolve local variability in that particular region or time frame. Such
515 differences likely arise from a combination of regional oceanographic complexity and satellite data limitations, including issues
516 related to proximity to sea ice or the presence of submesoscale activity not well resolved by gridded products.

517

518 **Table 2: Comparison of daily satellite-derived velocity to the ITP velocity along the ITP tracks. Correlations (*r*) with *p*<0.05 are in**
519 **bold. Numbers in the bracket are from the weekly mean timeseries.**

ITP-Vs		Mean (ITP)	Mean (Sat.)	STD (ITP)	STD (Sat.)	r	R^2
ITP-70	Zonal	-0.006	-0.006	0.022	0.014	**0.31 (0.45)**	0.12 (0.32)
	Meridional	-0.005	-0.003	0.021	0.015	**0.42 (0.59)**	0.20 (0.40)
ITP-77	Zonal	-0.022	-0.016	0.023	0.011	0.07 (0.31)	0.11 (0.20)
	Meridional	-0.005	-0.004	0.024	0.021	**0.37 (0.47)**	0.01 (0.02)
ITP-78	Zonal	-0.021	-0.011	0.022	0.014	**0.42 (0.78)**	0.32 (0.77)
	Meridional	-0.013	0.001	0.026	0.017	**0.43 (0.61)**	0.25 (0.32)
ITP-79	Zonal	-0.006	-0.007	0.024	0.013	**0.24** (0.38)	0.02 (0.11)
	Meridional	-0.020	-0.001	0.027	0.013	**0.56 (0.76)**	0.47 (0.60)
ITP-80	Zonal	-0.004	-0.001	0.020	0.012	**0.42 (0.61)**	0.30 (0.60)
	Meridional	-0.002	0.010	0.024	0.012	**0.34 (0.52)**	0.23 (0.16)
Mean	Zonal	-0.010	-0.008	0.022	0.011	0.29 (0.50)	0.13 (0.40)
	Meridional	-0.009	0.002	0.023	0.016	0.42 (0.59)	0.22 (0.28)

520

521
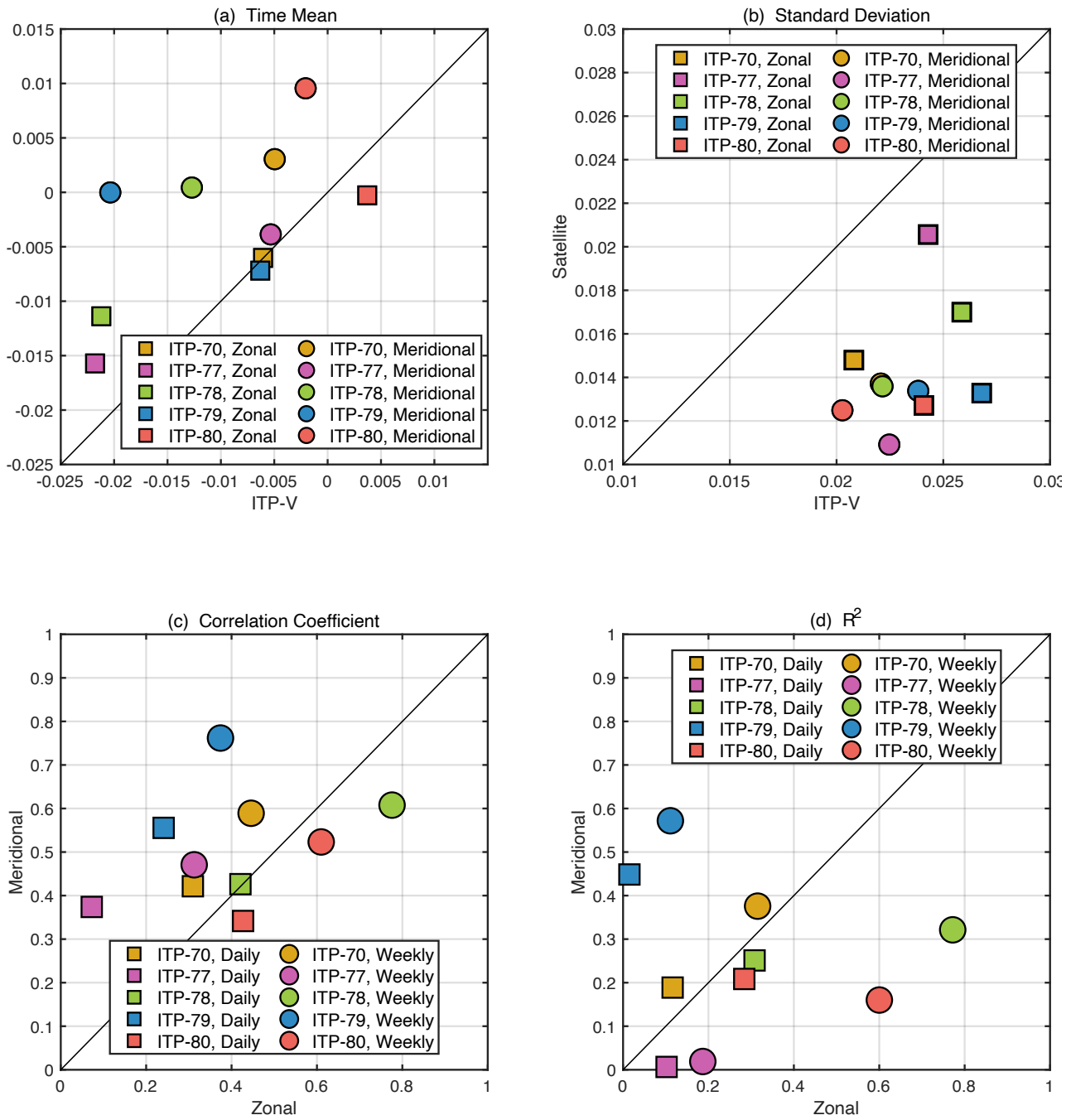
Figure 14: Scatterplots of statistics of satellite-derived velocity and the ITP velocity. (a) Temporal mean and (b) standard deviation of the paired velocity (unit: m/s). (c) Correlation between satellite-derived velocity and the ITP velocity. (d) Coefficient of determination (R^2) of the variation in the ITPs explained by satellite-derived velocity.

525

The comparison between satellite-derived ocean surface stress estimates and ITP observations, despite their differences in resolution and sampling, shows encouraging agreement at the first-order level. The satellite stress products successfully capture the broad spatial and temporal variability in surface velocity, supporting the utility of satellite-based estimates in reflecting first-order dynamical signals. This level of agreement supports the overall utility of satellite products in characterizing large-scale stress variability and motivates their continued use in data-sparse polar regions.

However, key limitations remain due to inherent mismatches in spatial and temporal sampling between the datasets. Satellite observations, with their typical resolution of ~25 km and daily sampling frequency, cannot resolve the submesoscale variability and high-frequency processes detectable in the pointwise and often sub-daily ITP profiles (Timmermans et al., 2008). This spatial averaging can smooth out gradients in wind, ice motion, or stress fields that may be sharply defined at smaller scales, particularly in regions such as the marginal ice zone (MIZ) where sea ice concentration and morphology are highly variable (Manucharyan & Thompson, 2017; Alberello et al., 2020).

Temporally, satellite-derived surface stress products may fail to capture transient forcing events such as storm-driven accelerations, inertial oscillations, or short-lived leads in sea ice. In contrast, ITPs can resolve such high-frequency processes (Toole et al., 2011; Timmermans et al., 2012), leading to potential discrepancies when aligning the two datasets. Furthermore, since satellite estimates of stress are often derived from independent wind and ice motion products (e.g., National Centers for Environmental Prediction Reanalysis, NSIDC drift), their accuracy is subject to the limitations of those input fields (Sumata et al., 2014; Lavergne et al., 2010). The lack of fully collocated wind and ice motion fields at the exact time and location of ITP measurements compounds the uncertainty.

These spatial and temporal mismatches further introduce representation errors, as mismatches are not due to sensor or algorithm flaws but rather due to sampling disparities (Janjić et al., 2008). Such errors have been well documented in the context of satellite sea surface salinity (Boutin et al., 2016; Vinogradova et al., 2019). These limitations are evident in the reduced agreement observed for ITP-77, ITP-78, and ITP-79, where several compounding factors likely contributed. First, the ~25 km resolution of the satellite product may be insufficient to resolve submesoscale features and sharp velocity gradients. Second, the timing of deployment in March overlaps with a period of elevated kinetic energy in the Beaufort Gyre (Cassianides et al., 2023), during which intensified eddy activity in the Canada Basin enhances mesoscale variability (Son et al., 2022; Regan et al., 2020). This variability, well captured by the high-resolution ITP profiles, is easily aliased or smoothed out in the satellite-derived daily fields, further amplifying mismatches in direct comparisons.

Moving forward, best practices in validation should account for these differences explicitly. The development of higher-resolution satellite products (Auger et al., 2022; Lucas et al., 2023), along with assimilation into coupled models (Wang et al., 2018), also offers a promising path forward. Increased density of ITP deployments, moored arrays, and coordinated airborne campaigns (Perovich et al., 2023) will be crucial for better spatial coverage in dynamic regions like the Beaufort Gyre and the MIZ.

In conclusion, the comparison reveals that while satellite-derived velocities are subject to systematic biases and reduced variability relative to in situ observations, they nonetheless capture a significant portion of the observed variance, particularly

when considered at weekly timescales. The agreement is stronger for the meridional component and in regions where large-scale geostrophic flows dominate. These results support the use of satellite-derived velocity products for basin-scale circulation studies, while also highlighting the need for caution in applications requiring high-frequency or fine-scale flow resolution.

5 Data Availability

Daily fields of ocean-surface stress vectors and derived vertical Ekman velocity for the polar oceans are provided for two periods: 2011–2018 for the Arctic (EPSG number 3408) and 2013–2018 for the Antarctic (EPSG number 3409) and are available at https://doi.org/10.5281/zenodo.14750492 (Liu & Yu, 2024). The datasets include three auxiliary fields: (i) land mask, (ii) grid longitudes and latitudes, and (iii) uncertainty estimates for ocean-surface stress.

The input datasets can be found at NSIDC (ice motion: https://nsidc.org/data/nsidc-0116/versions/4; ice extent: https://nsidc.org/data/nsidc-0051/versions/2) and AVISO website (dynamic topography: https://www.aviso.altimetry.fr/en/data/products/sea-surface-height-products/regional/arctic-ocean-sea-level-heights.html).

ITP-V data used in this work are retrieved from the WHOI website at https://www2.whoi.edu/site/itp/. CPOM-DOT/geostrophic currents data are provided by the Centre for Polar Observation and Modelling, University College London (https://www.cpom.ucl.ac.uk/dynamic_topography). The associated scripts and packages used in this study are openly available on GitHub at (https://github.com/cydenyliu/Polar_Stress).

6 Conclusions

This work presents a daily, 25 km resolution dataset of satellite-derived ocean-surface stress for the Arctic (2011-2018) and Southern Oceans (2013-2018). The dataset provides detailed daily maps of τ_o across polar regions north of 60°N and south of 50°S. This dataset achieves finer spatial and temporal resolution, enabling more precise analysis of short-term air-sea interactions and regional Ekman dynamics. In both the Arctic and Antarctic, it captures short-term and sharp transition between Ekman upwelling in ice-free regions and downwelling in ice-covered areas.

Uncertainty in the derived ocean-surface stress fields arises primarily from two sources. The first is the spatial filter applied to the SSH datasets, which reduces small scale variability and enhances consistency between the sea level fields. The second source of uncertainty is related to the ice-water drag coefficient, which is poorly observed and can vary significantly between order of 10^{-3} and 10^{-2}. These factors result in a median uncertainty of approximately 20% in the Arctic and about 40% in the Southern Ocean.

The derived Ekman velocity is used to validate against ITP data from the Arctic's Canada Basin. Satellite-derived surface velocity, which combine Ekman and geostrophic components, capture over 50% of the observed variation in surface velocity. Correlation coefficients range from 0.6 to 0.8 on monthly and longer timescales, indicating moderate to strong agreement. It is important to consider the complex dynamics of the Arctic Ocean when interpreting these statistics. In addition to Ekman

and geostrophic velocity (Regan et al., 2019), processes such as shallow eddy activity (Timmermans et al., 2008; Kenigson et al., 2021; Meneghello et al., 2021), turbulent mixing (Guthrie et al., 2013; Kawaguchi et al., 2014, 2019), and internal waves (Kawaguchi et al., 2016; Zhao et al., 2016) also contribute to the observed variability. Many of these processes remain challenging to observe and parameterize.

Future updates will focus on two primary areas. We plan to extend the dataset's temporal coverage through 2021 by incorporating updated versions of OAFlux and other relevant data products as they become available. This will ensure consistency across components while maintaining the dataset's reliability. Second, the availability of reliable surface height products for the polar region will further enhance data accuracy. While awaiting these advancements, we will assess the potential impacts of transitioning to reanalysis data on our results. Additionally, future research will address key processes that remain underrepresented, such as variable Ekman depth and mesoscale turbulence, to refine the depiction of polar ocean dynamics. Incorporating these factors will improve the ability to capture localized features critical for understanding air-ice-ocean interactions.

Appendix A: Glossary of Terminology

Table A1: glossary of terminology and acronyms used in this study.

Terminology/Acronyms	Description
EASE	Equal-Area Scalable Earth grid
SSH	Sea Surface Height
OAFlux	Objectively Analyzed Air-Sea Fluxes
NSIDC	National Snow and Ice Data Center
MEaSUREs	Making Earth System Data Records for Use in Research Environments
COARE	Coupled Ocean–Atmosphere Response Experiment
SSM/I	Special Sensor Microwave/Imager
AMSR-E	Advanced Microwave Scanning Radiometer for EOS
AVHRR	Advanced Very High Resolution Radiometer
MODIS	Moderate Resolution Imaging Spectroradiometer
QuikSCAT	Quick Scatterometer
IABP	International Arctic Buoy Programme
CLS/PML	Collecte Localisation Satellites / Plymouth Marine Laboratory
SMMR	Scanning Multichannel Microwave Radiometer

DMSP	Defense Meteorological Satellite Program
SSM	Special Sensor Microwave
I-SSMIS	Improved Special Sensor Microwave Imager/Sounder
RMSD	Root Mean Square Deviation
CPOM	Centre for Polar Observation and Modelling
DOT	Dynamic Ocean Topography
SIZ	Seasonal Ice Zone
PIZ	Perennial Ice Zone
MIZ	Marginal Ice Zone
STD	Standard Deviation
R²	Coefficient of Determination
ITP	Ice-Tethered Profiler

605

Author contributions

607 CL: conceptualization, data curation, formal analysis, methodology, software, visualization, writing – original draft preparation,
608 writing – review and editing. LY: conceptualization, project administration, supervision, validation, writing – review and
609 editing.

Competing interests

611 The contact author has declared that none of the authors has any competing interests.

Finance Support

613 This project is supported by NASA under grant no. 80NSSC23K0981.

References

615 Alberello, A., Bennetts, L., Heil, P., Eayrs, C., Vichi, M., MacHutchon, K., Onorato, M. and Toffoli, A.. Drift of pancake ice
616 floes in the winter Antarctic marginal ice zone during polar cyclones. Journal of Geophysical Research: Oceans, 125(3),
617 p.e2019JC015418, 2020.

618 Anderson, M. R.: The onset of spring melt in first-year ice regions of the Arctic as determined from scanning multichannel

619 microwave radiometer data for 1979 and 1980. Journal of Geophysical Research: Oceans, 92(C12), 13153-13163, 1987.

620 Armitage, T. W., Bacon, S., Ridout, A. L., Thomas, S. F., Aksenov, Y., & Wingham, D. J.: Arctic sea surface height variability

621 and change from satellite radar altimetry and GRACE, 2003–2014. Journal of Geophysical Research: Oceans, 121(6), 4303-

622 4322, 2016.

623 Armitage, T. W. K., Bacon, S., Ridout, A. L., Petty, A. A., Wolbach, S., and Tsamados, M.: Arctic Ocean surface geostrophic

624 circulation 2003–2014, The Cryosphere, 11, 1767– 1780, https://doi.org/10.5194/tc-11-1767-2017, 2017.

625 Auger M, Prandi P, Sallée J B. Southern ocean sea level anomaly in the sea ice-covered sector from multimission satellite

626 observations. Scientific Data, 9(1): 70, 2022.

627 Brenner, S., Rainville, L., Thomson, J., Cole, S. and Lee, C. Comparing observations and parameterizations of ice-ocean drag

628 through an annual cycle across the Beaufort Sea. Journal of Geophysical Research: Oceans, 126(4), p.e2020JC016977, 2021.

629 Boutin, J., Chao, Y., Asher, W.E., Delcroix, T., Drucker, R., Drushka, K., Kolodziejczyk, N., Lee, T., Reul, N., Reverdin, G.

630 and Schanze, J.. Satellite and in situ salinity: Understanding near-surface stratification and subfootprint variability. Bulletin of

631 the American Meteorological Society, 97(8), pp.1391-1407, 2016.

632 Boutin, G., Lique, C., Ardhuin, F., Rousset, C., Talandier, C., Accensi, M. and Girard-Ardhuin, F.. Towards a coupled model

633 to investigate wave–sea ice interactions in the Arctic marginal ice zone. The Cryosphere, 14(2), pp.709-735, 2020.

634 Campbell EC, Wilson EA, Moore GK, Riser SC, Brayton CE, Mazloff MR, Talley LD. Antarctic offshore polynyas linked to

635 Southern Hemisphere climate anomalies. Nature. 570(7761):319-25, 2019.

636 Cassianides, A., Lique, C., Tréguier, A. M., Meneghello, G., & De Marez, C.: Observed Spatio-Temporal Variability of the

637 Eddy-Sea Ice Interactions in the Arctic Basin. Journal of Geophysical Research: Oceans, 128(6), e2022JC019469, 2023.

638 Cavalieri, D. J., C. L. Parkinson, P. Gloersen, and H. J. Zwally: Sea ice concentrations from Nimbus-7 SMMR and DMSP

639 SSM/I-SSMIS passive microwave data, version 1. NSIDC, https://doi.org/10.5067/ 8GQ8LZQVL0VL., 1996

640 Cole, S. T., & Stadler, J.: Deepening of the winter mixed layer in the Canada basin, Arctic Ocean over 2006–2017. Journal of

641 Geophysical Research: Oceans, 124(7), 4618-4630, 2019.

642 Cole, S. T., M.-L. Timmermans, J. M. Toole, R. A. Krishfield, and F. T. Thwaites: Ekman veering, internal waves, and

643 turbulence observed under Arctic sea ice. J. Phys. Oceanogr., 44, 1306–1328, https://doi.org/10.1175/JPO-D-12-0191.1, 2014.

644 DiGirolamo, N. E., C. L. Parkinson, D. J. Cavalieri, P. Gloersen, and H. J. Zwally.: updated yearly. Sea Ice Concentrations

645 from Nimbus-7 SMMR and DMSP SSM/I-SSMIS Passive Microwave Data, Version 2. Boulder, Colorado USA. NASA

646 National Snow and Ice Data Center Distributed Active Archive Center. https://doi.org/10.5067/MPYG15WAA4WX, 2022.

647 Eayrs, C., Holland, D. M., Francis, D., Wagner, T. J. W., Kumar, R., & Li, X. Understanding the seasonal cycle of Antarctic

648 sea ice extent in the context of longer-term variability. Reviews of Geophysics. 57, 1037–1064, 2019

649 Fairall, C. W., Bradley, E. F., Hare, J. E., Grachev, A. A., & Edson, J. B.: Bulk parameterization of air–sea fluxes: Updates

650 and verification for the COARE algorithm. Journal of climate, 16(4), 571-591, 2003.

651 Guest, P. S., & Davidson, K. L.: The effect of observed ice conditions on the drag coefficient in the summer East Greenland
652 Sea marginal ice zone. Journal of Geophysical Research: Oceans, 92(C7), 6943-6954, 1987.

653 Guest, P. S., and Davidson, K. L.: The aerodynamic roughness of different types of sea ice, J. Geophys. Res., 96(C3), 4709–
654 4721, 1991.

655 Guthrie, J. D., Morison, J. H., & Fer, I.: Revisiting internal waves and mixing in the Arctic Ocean. Journal of Geophysical
656 Research: Oceans, 118(8), 3966-3977, 2013.

657 Ivanova, N., Pedersen, L.T., Tonboe, R.T., Kern, S., Heygster, G., Lavergne, T., Sørensen, A., Saldo, R., Dybkjær, G., Brucker,
658 L.J.T.C. and Shokr, M.. Inter-comparison and evaluation of sea ice algorithms: towards further identification of challenges
659 and optimal approach using passive microwave observations. The Cryosphere, 9(5), pp.1797-1817, 2015.

660 Janjić, T., Bormann, N., Bocquet, M., Carton, J.A., Cohn, S.E., Dance, S.L., Losa, S.N., Nichols, N.K., Potthast, R., Waller,
661 J.A. and Weston, P. On the representation error in data assimilation. Quarterly Journal of the Royal Meteorological Society,
662 144(713), pp.1257-1278, 2018..

663 Kawaguchi, Y., Hoppmann, M., Shirasawa, K. et al. Dependency of the drag coefficient on boundary layer stability beneath
664 drifting sea ice in the central Arctic Ocean. Sci Rep 14, 15446, 2024

665 Kawaguchi, Y., Itoh, M., Fukamachi, Y., Mori,ya, E., Onodera, J., Kikuchi, T., & Harada, N.: Year-round observations of sea-
666 ice drift and near-inertial internal waves in the Northwind Abyssal Plain, Arctic Ocean. Polar Science, 21, 212-223, 2019.

667 Kawaguchi, Y., Kikuchi, T., & Inoue, R.: Vertical heat transfer based on direct microstructure measurements in the ice-free
668 Pacific-side Arctic Ocean: the role and impact of the Pacific water intrusion. Journal of oceanography, 70, 343-353, 2014.

669 Kawaguchi, Y., Nishino, S., Inoue, J., Maeno, K., Takeda, H., & Oshima, K.: Enhanced diapycnal mixing due to near-inertial
670 internal waves propagating through an anticyclonic eddy in the ice-free Chukchi Plateau. Journal of Physical Oceanography,
671 46(8), 2457-2481, 2016.

672 Kenigson, J.S., Gelderloos, R. and Manucharyan, G.E., Vertical structure of the Beaufort Gyre halocline and the crucial role
673 of the depth-dependent eddy diffusivity. Journal of Physical Oceanography, 51(3), pp.845-860. 2021.

674 Krishfield, R., Toole, J., Proshutinsky, A., & Timmermans, M. L.: Automated ice-tethered profilers for seawater observations
675 under pack ice in all seasons. Journal of Atmospheric and Oceanic Technology, 25(11), 2091-2105, 2008.

676 Lavergne, T., Eastwood, S., Teffah, Z., Schyberg, H. and Breivik, L.A.. Sea ice motion from low-resolution satellite sensors:
677 An alternative method and its validation in the Arctic. Journal of Geophysical Research: Oceans, 115(C10) , 2010.

678 Lefebvre, W., Goosse, H., Timmermann, R. and Fichefet, T., Influence of the Southern Annular Mode on the sea ice–ocean
679 system. Journal of Geophysical Research: Oceans, 109(C9). 2004.

680 Lin, P., Pickart, R.S., Heorton, H., Tsamados, M., Itoh, M. and Kikuchi, T.: Recent state transition of the Arctic Ocean's
681 Beaufort Gyre. Nature Geoscience, 16(6), pp.485-491, 2023.

682 Liu, C., and Yu, L.: Arctic/Antarctic Ocean-Surface Stress Analysis, 2011-2018/2013-2018, Zenodo [data set],
683 https://doi.org/10.5281/zenodo.14750492, 2024.

684 Lucas, S., Johannessen, J.A., Cancet, M., Pettersson, L.H., Esau, I., Rheinlænder, J.W., Ardhuin, F., Chapron, B., Korosov,

685 A., Collard, F. and Herlédan, S.. Knowledge gaps and impact of future satellite missions to facilitate monitoring of changes in

686 the Arctic Ocean. Remote Sensing, 15(11), p.2852, 2023.

687 Lüpkes, C., & Birnbaum, G.: Surface drag in the Arctic marginal sea-ice zone: A comparison of different parameterisation

688 concepts. Boundary-layer meteorology, 117, 179-211, 2005.

689 Lüpkes, C., Gryanik, V. M., Hartmann, J., & Andreas, E. L.: A parametrization, based on sea ice morphology, of the neutral

690 atmospheric drag coefficients for weather prediction and climate models. Journal of Geophysical Research: Atmospheres,

691 117(D13), 2012.

692 Lüpkes, C. and Gryanik, V.M.: A stability-dependent parametrization of transfer coefficients for momentum and heat over

693 polar sea ice to be used in climate models. Journal of Geophysical Research: Atmospheres, 120(2), pp.552-581, 2015.

694 Ma, B., M. Steele, and C. M. Lee: Ekman circulation in the Arctic Ocean: Beyond the Beaufort Gyre. J. Geophys. Res. Oceans,

695 122, 3358–3374, https://doi.org/10.1002/2016JC012624, 2017.

696 Manucharyan, G.E. and Thompson, A.F.. Submesoscale sea ice-ocean interactions in marginal ice zones. Journal of

697 Geophysical Research: Oceans, 122(12), pp.9455-9475, 2017.

698 Martin, T., Steele, M. and Zhang, J., Seasonality and long-term trend of Arctic Ocean surface stress in a model. Journal of

699 Geophysical Research: Oceans, 119(3), pp.1723-1738. 2014.

700 Martin, T., Tsamados, M., Schroeder, D. & Feltham, D. L. The impact of variable sea ice roughness on changes in arctic ocean

701 surface stress: A model study. J. Geophys. Res.: Oceans 121, 1931–1952, 2016.

702 McPhee, M. G. Air-ice-ocean interaction—Turbulent ocean boundary layer exchange processes (Springer, New York, 2008).

703 McPhee, M. G.: Intensification of geostrophic currents in the Canada Basin, Arctic Ocean. J. Climate, 26, 3130–3138, https://

704 doi.org/10.1175/JCLI-D-12-00289.1, 2013.

705 Meehl, G. A. et al. Sustained ocean changes contributed to sudden Antarctic sea ice retreat in late 2016. Nat. Commun. 10, 14,

706 2019.

707 Meneghello, G., J. Marshall, S. T. Cole, and M.-L. Timmermans: Observational inferences of lateral eddy diffusivity in the

708 halocline of the Beaufort Gyre. Geophys. Res. Lett., 44, 12 331–12 338, 2017.

709 Meneghello, G., Marshall, J., Lique, C., Isachsen, P.E., Doddridge, E., Campin, J.M., Regan, H. and Talandier, C., Genesis

710 and decay of mesoscale baroclinic eddies in the seasonally ice-covered interior Arctic Ocean. Journal of Physical

711 Oceanography, 51(1), pp.115-129. 2021.

712 Meneghello, G., Marshall, J., Timmermans, M. L., & Scott, J.: Observations of seasonal upwelling and downwelling in the

713 Beaufort Sea mediated by sea ice. Journal of Physical Oceanography, 48(4), 795-805, 2018.

714 Meier, W.N.. Comparison of passive microwave ice concentration algorithm retrievals with AVHRR imagery in Arctic

715 peripheral seas. IEEE Transactions on geoscience and remote sensing, 43(6), pp.1324-1337, 2005.

716 Moore, G.W.K., Steele, M., Schweiger, A.J., Zhang, J. and Laidre, K.L.. Thick and old sea ice in the Beaufort Sea during

717 summer 2020/21 was associated with enhanced transport. *Communications Earth & Environment*, *3*(1), p.198, 2022.

Muilwijk, M., Hattermann, T., Martin, T. and Granskog, M.A.. Future sea ice weakening amplifies wind-driven trends in surface stress and Arctic Ocean spin-up. Nature Communications, 15(1), p.6889, 2024.

Overland, J. E.: Atmospheric boundary layer structure and drag coefficients over sea ice, J. Geophys. Res., 90(C5), 9029–9049, 1985.

Park, H.S., Stewart, A.L. and Son, J.H., Dynamic and thermodynamic impacts of the winter Arctic Oscillation on summer sea ice extent. Journal of Climate, 31(4), pp.1483-1497. 2018.

Parkinson, C. L.: A 40-y record reveals gradual Antarctic sea ice increases followed by decreases at rates far exceeding the rates seen in the Arctic. Proceedings of the National Academy of Sciences, 116(29), 14414-14423, 2019.

Perovich, D., Raphael, I., Moore, R., Clemens-Sewall, D., Lei, R., Sledd, A. and Polashenski, C.. Sea ice heat and mass balance measurements from four autonomous buoys during the MOSAiC drift campaign. Elementa: Science of the Anthropocene, 11(1), 2023.

Prandi, P., Poisson, J.-C., Faugère, Y., Guillot, A., and Dibarboure, G.: Arctic sea surface height maps from multi-altimeter combination, Earth Syst. Sci. Data, 13, 5469–5482, https://doi.org/10.5194/essd-13-5469-2021, 2021

Purich, A. and Doddridge, E.W., Record low Antarctic sea ice coverage indicates a new sea ice state. Communications Earth & Environment, 4(1), p.314. 2023.

Regan, H. C., Lique, C., and Armitage, T. W. K.: The Beaufort Gyre Extent, Shape, and Location Between 2003 and 2014 From Satellite Observations, J. Geophys. Res.-Oceans, 124, 844–862, 2019.

Regan, H., Lique, C., Talandier, C., and Meneghello, G.: Response of total and eddy kinetic energy to the recent spin up of the Beaufort Gyre, J. Phys. Oceanogr., 50, 575–594, 2020.

Rigor, I.G., Wallace, J.M. and Colony, R.L.. Response of sea ice to the Arctic Oscillation. Journal of Climate, 15(18), pp.2648-2663, 2002.

Son, E.Y., Kawaguchi, Y., Cole, S.T., Toole, J.M. and Ha, H.K.. Assessment of Turbulent Mixing Associated With Eddy-Wave Coupling Based on Autonomous Observations From the Arctic Canada Basin. Journal of Geophysical Research: Oceans, 127(9), p.e2022JC018489, 2022.

Stammerjohn, S., Massom, R. A., Rind, D. & Martinson, D. G. Regions of rapid sea ice change: an inter-hemispheric seasonal comparison. Geophys. Res. Lett. 39, L06501 (2012).

Sterlin, J., Tsamados, M., Fichefet, T., Massonnet, F. and Barbic, G., Effects of sea ice form drag on the polar oceans in the NEMO-LIM3 global ocean–sea ice model. Ocean Modelling, 184, p.102227, 2023.

Stroeve, J., & Notz, D.: Changing state of Arctic sea ice across all seasons. Environmental Research Letters, 13(10), 103001, 2018.

Sumata H, Lavergne T, Girard-Ardhuin F, Kimura N, Tschudi MA, Kauker F, Karcher M, Gerdes R. An intercomparison of Arctic ice drift products to deduce uncertainty estimates. Journal of Geophysical Research: Oceans. Aug;119(8):4887-921, 2014.

751 Thorndike, A.S. and Colony, R., Sea ice motion in response to geostrophic winds. Journal of Geophysical Research:
752 Oceans, 87(C8), pp.5845-5852. 1982.

753 Thouvenin-Masson, C., Boutin, J., Vergely, J.L., Reverdin, G., Martin, A.C., Guimbard, S., Reul, N., Sabia, R., Catany, R.
754 and Hembise Fanton-d'Andon, O.. Satellite and in situ sampling mismatches: Consequences for the estimation of satellite sea
755 surface salinity uncertainties. Remote Sensing, 14(8), p.1878, 2022.

756 Timmermans, M.L., Cole, S. and Toole, J.. Horizontal density structure and restratification of the Arctic Ocean surface layer.
757 Journal of Physical Oceanography, 42(4), pp.659-668, 2012.

758 Timmermans, M. L., Toole, J., Proshutinsky, A., Krishfield, R., & Plueddemann, A.: Eddies in the Canada Basin, Arctic Ocean,
759 observed from ice-tethered profilers. Journal of Physical Oceanography, 38(1), 133-145, 2008.

760 Toole, J. M., R. A. Krishfield, M.-L. Timmermans, and A. Proshutinsky: The ice-tethered profiler: Argo of the Arctic.
761 Oceanography, 24 (3), 126–135, 2011.

762 Tsamados, M., Feltham, D.L., Schroeder, D., Flocco, D., Farrell, S.L., Kurtz, N., Laxon, S.W. and Bacon, S.. Impact of variable
763 atmospheric and oceanic form drag on simulations of Arctic sea ice. Journal of Physical Oceanography, 44(5), pp.1329-1353,
764 2014.

765 Tschudi, M. A., Meier, W. N., & Stewart, J. S.: An enhancement to sea ice motion and age products at the National Snow and
766 Ice Data Center (NSIDC). The Cryosphere, 14(5), 1519-1536, 2020.

767 Tschudi, M., Meier, W. N., Stewart, J. S., Fowler, C., and Maslanik, J.: Polar Pathfinder Daily 25 km EASE-Grid Sea Ice
768 Motion Vectors, Version 4, Boulder, CA, USA, NASA National Snow and Ice Data Center Distributed Active Archive Center,
769 2019.

770 Turner J, Holmes C, Caton Harrison T, Phillips T, Jena B, Reeves-Francois T, Fogt R, Thomas ER, Bajish CC. Record low
771 Antarctic sea ice cover in February 2022. Geophysical Research Letters. 49(12):e2022GL098904, 2022.

772 Vinogradova, N.T. and Ponte, R.M.. Small-scale variability in sea surface salinity and implications for satellite-derived
773 measurements. Journal of Atmospheric and Oceanic Technology, 30(11), pp.2689-2694, 2013.

774 Vinogradova, N., Lee, T., Boutin, J., Drushka, K., Fournier, S., Sabia, R., Stammer, D., Bayler, E., Reul, N., Gordon, A. and
775 Melnichenko, O.. Satellite salinity observing system: Recent discoveries and the way forward. Frontiers in Marine Science, 6,
776 p.243, 2019.

777 Wang X, Chen R, Li C, Chen Z, Hui F, Cheng X. An intercomparison of satellite derived Arctic sea ice motion products.
778 Remote Sensing, 14(5):1261, 2022.

779 Wang, Q., Wekerle, C., Danilov, S., Wang, X. and Jung, T.. A 4.5 km resolution Arctic Ocean simulation with the global
780 multi-resolution model FESOM 1.4. Geoscientific Model Development, 11(4), pp.1229-1255, 2018.

781 Wang, M., König, M. and Oppelt, N.. Partial shape recognition for sea ice motion retrieval in the marginal ice zone from
782 Sentinel-1 and Sentinel-2. Remote Sensing, 13(21), p.4473, 2021.

783 Wu, Y., Wang, Z. and Liu, C.. Impacts of changed ice-ocean stress on the North Atlantic Ocean: Role of ocean surface currents.
784 Frontiers in Marine Science, 8, p.628892, 2021.

785 Yang, J.: Seasonal and interannual variability of downwelling in the Beaufort Sea. J. Geophys. Res., 114, C00A14, https://

786 doi.org/10.1029/2008JC005084, 2009.

787 Yang, J.: The seasonal variability of the Arctic Ocean Ekman transport and its role in the mixed layer heat and salt fluxes. J.

788 Climate, 19, 5366–5387, https://doi.org/10.1175/ JCLI3892.1, 2006.

789 Yu, L., & Jin, X.: Insights on the OAFlux ocean surface vector wind analysis merged from scatterometers and passive

790 microwave radiometers (1987 onward). Journal of Geophysical Research: Oceans, 119(8), 5244-5269, 2014a.

791 Yu, L., & Jin, X.: Confidence and sensitivity study of the OAFlux multisensor synthesis of the global ocean surface vector

792 wind from 1987 onward. Journal of Geophysical Research: Oceans, 119(10), 6842-6862, 2014b.

793 Yu, L.: Global air–sea fluxes of heat, fresh water, and momentum: Energy budget closure and unanswered questions. Annual

794 Review of Marine Science, 11(1), 227–248. https://doi.org/10.1146/annurev-marine-010816-060704, 2019.

795 Zhao, M., Timmermans, M.-L., Cole, S., Krishfield, R., and Toole, J.: Evolution of the eddy field in the Arctic Ocean's Canada

796 Basin, 2005–2015, Geophys. Res. Lett., 43, 8106–8114, https://doi.org/10.1002/2016GL069671, 2016.

797 Zhong, W., Steele, M., Zhang, J. and Zhao, J.. Greater role of geostrophic currents in Ekman dynamics in the western Arctic

798 Ocean as a mechanism for Beaufort Gyre stabilization. Journal of Geophysical Research: Oceans, 123(1), pp.149-165, 2018.